Burns & Trauma, 2026, 14, tkag020
https://doi.org/10.1093/burnst/tkag020
Published: 12 March 2026
Research Article

OXFORD

Targeting the Jun-Irf8-CD36 axis attenuates fibrotic scar formation and promotes functional recovery after spinal cord injury

Min Feng[1,‡], JiYu Li[1,2,‡], Jieying Zhang[3,‡], Hang Zhang[4,‡], Wanhua Li[3,‡], Yili Liu[3], Xiang Gao[5], Hanyue Yang[3], Zeyu Liu[6], Chong Gao[6], Ruiyang Xiao[3], Jianru Xiao[1], Xiaozhong Zhou[5], Leilei Gong[3,*], Songlin Zhou[3,*], Jian Zhao[1,*], Caiqi Cheng[7,*]

[1]Orthopaedic Oncology Center, Department of Orthopaedics, Changzheng Hospital, Second Military Medical University, No. 415 Fengyang Road, Huangpu District, Shanghai, 200003, China
[2]Department of Orthopedics, Huashan Hospital, Fudan University, No. 12 Middle Wulumuqi Road, Jing'an District, Shanghai, 200040, China
[3]Jiangsu Key Laboratory of Tissue Engineering and Neuroregeneration, Key Laboratory of Neuroregeneration of Ministry of Education, Coinnovation Center of Neuroregeneration, NMPA Key Laboratory for Research and Evaluation of Tissue Engineering Technology Products, Nantong University, No. 19 Qixiu Road, Nantong, 226001, Jiangsu, China
[4]Department of Rehabilitation Medicine, The Second Affiliated Hospital of Nantong University, Nantong First People's Hospital, No. 666 Shengli Road, Nantong, Jiangsu, 226000, China
[5]Department of Orthopedics, The Second Affiliated Hospital of Soochow University, No. 1055 Sanxiang Road, Suzhou, Jiangsu, 215004, China
[6]Nantong University School of Medicine, Nantong University, No. 19 Qixiu Road, Nantong, Jiangsu, 226001, China
[7]Department of Orthodontics, Shanghai Ninth People's Hospital, Shanghai Jiao Tong University School of Medicine, No. 500 Quxi Road, Shanghai 200011, China

*Corresponding authors. Caiqi Cheng, E-mail: caiqi_cheng@shsmu.edu.cn; Jian Zhao, E-mail: drzhaojian@189.cn; Songlin Zhou, E-mail: songlin.zhou@ntu.edu.cn; Leilei Gong, E-mail: gonglei@ntu.edu.cn
‡These authors contributed equally to this work.

Abstract

Background: **Fibrotic scar formation constitutes a significant pathological obstacle that impedes neural regeneration and long-term functional recovery following spinal cord injury (SCI). However, the spatial distribution of key pro-fibrotic mediators within lesion scars and the upstream regulatory mechanisms driving fibroblast activation remain inadequately defined. This study aims to characterize CD36-associated fibrotic remodeling after SCI and to determine whether targeting the c-Jun–Irf8–CD36 axis could attenuate scar formation, improve the regenerative microenvironment, and promote functional recovery.**

Methods: **This study integrated single-cell ribonucleic acid sequencing and spatial transcriptomic profiling to characterize CD36 expression patterns and identify fibroblast subpopulations within SCI scars. Pharmacological interventions were administered in mouse SCI models, using salvianolic acid B (SAB) to inhibit CD36 and T5224 to block AP-1/c-Jun activity. Histological and immunofluorescence analyses were performed to assess fibroblast accumulation, extracellular matrix deposition, angiogenesis, and axonal regeneration, alongside longitudinal behavioral evaluations of locomotor function. Mechanistic validation of the regulatory pathway was achieved through CUT&Tag and dual-luciferase reporter assays to investigate c-Jun–Irf8–CD36 transcriptional regulation, complemented by integrated single-cell/spatial analyses to assess fibroblast subcluster remodeling post-treatment.**

Results: **Spatial and single-cell analyses demonstrated that CD36 is predominantly localized within lesion scars, correlating with fibrotic progression and preferentially upregulated in specific fibroblast subclusters. SAB-mediated CD36 inhibition markedly reduced $P4HB^{+}$ fibroblast accumulation, alleviated fibrotic deposition, enhanced angiogenesis and axonal regeneration, and improved hindlimb functional recovery. Mechanistically, c-Jun was upregulated in scar regions and indirectly promoted CD36 transcription through Irf8 activation, establishing a c-Jun–Irf8–CD36 signaling axis. CUT&Tag and reporter assays confirmed c-Jun binding to the Irf8 promoter, leading to Irf8-driven CD36 transcription. Similarly, T5224 downregulated CD36 expression, reduced fibroblast aggregation and matrix deposition, facilitated vascular remodeling, and promoted early functional recovery. These findings demonstrate that modulating this signaling pathway can significantly inhibit pathological scar formation and facilitate approximately scar-free healing, thereby providing an ideal microenvironment for tissue**

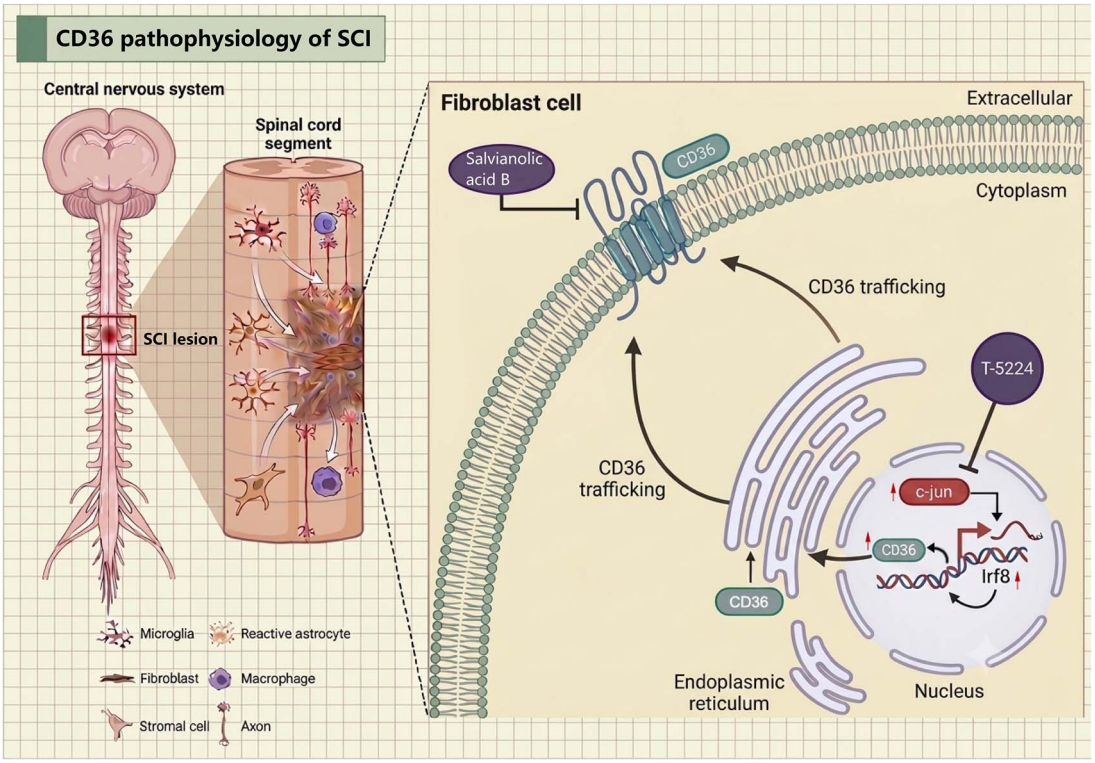
Received: 27 November 2025. **Revised:** 27 February 2026. **Accepted:** 8 March 2026
© The Author(s) 2026. Published by Oxford University Press.
This is an Open Access article distributed under the terms of the Creative Commons Attribution-NonCommercial License (https://creativecommons.org/licenses/by-nc/4.0/), which permits non-commercial re-use, distribution, and reproduction in any medium, provided the original work is properly cited. For commercial re-use, please contact reprints@oup.com for reprints and translation rights for reprints. All other permissions can be obtained through our RightsLink service via the Permissions link on the article page on our site—for further information please contact journals.permissions@oup.com.

Downloaded from academic.oup.com/burnstrauma/article/doi/10.1093/burnst/tkag020/8516470 by guest on 12 October 2026

regeneration. Multi-omic analyses further revealed that T5224 selectively inhibited the aberrant expansion of CD36^{+} fibroblast subclusters and reprogrammed their transcriptional states toward a less fibrotic phenotype.

Conclusions: **The c-Jun–Irf8–CD36 axis serves as a pivotal regulator of fibrotic scar formation after SCI. Targeting this pathway through CD36 inhibition (SAB) or AP-1/c-Jun blockade (T5224) attenuates fibrosis, remodels the scar microenvironment, enhances tissue repair, and promotes functional recovery, highlighting a promising therapeutic strategy for central nervous system injury.**

Graphical abstract



Keywords Single nucleus RNA sequencing, Spatial transcriptome, Spinal cord injury, Glial scar, Microenvironment, CD36, Salvianolic acid, T5224, c-Jun, Irf8

Highlights

- **Multi-omics analysis revealed the spatial distribution of CD36 was associated with fibrotic progression.**
- **Inhibition of CD36 using salvianolic acid B or the AP-1 inhibitor T5224 significantly reduced P4HB^{+} fibroblast accumulation.**
- **The c-Jun-Irf8-CD36 axis served as a critical regulator of fibrotic scar formation after spinal cord injury.**

Background

Spinal cord injury (SCI) is a severe trauma often accompanied by significant motor and sensory deficits, profoundly impacting patients' quality of life [1]. The acute phase, typically defined as the first 1–2 weeks following injury, represents a critical therapeutic window, which can be further divided into an early acute stage (2 h to 48 h post-injury) and a subacute stage [2 to 14 days post-injury (dpi)]. Timely intervention during this period can significantly reduce secondary injury and improve prognosis [2, 3]. Current treatment strategies primarily focus on stabilizing vital signs and preventing secondary damage, with corticosteroids and early surgical decompression being the most commonly employed approaches [4–7]. However, while these interventions can mitigate inflammation and relieve mechanical compression, they fail to address the pathological barriers at the lesion site, thus limiting long-term functional recovery.

Scar formation is a major obstacle to effective repair following SCI [8]. In the early acute phase, astrocytes are rapidly activated, forming a 'glial barrier' that limits the spread of inflammation while simultaneously secreting chondroitin sulfate proteoglycans (CSPGs), which inhibit axonal regeneration [9–12]. During the

Downloaded from academic.oup.com/burnstrauma/article/doi/10.1093/burnst/tkag020/8516470 by guest on 12 October 2026

late acute phase, disruption of the blood–brain barrier (BBB) and persistent inflammatory responses facilitate the infiltration of fibroblasts from perivascular cells, meningeal cells, and bone marrow. These fibroblasts deposit extracellular matrix (ECM) proteins, contributing to the formation of fibrotic scars [13]. Although these scars provide structural stability to the lesion site, they also represent significant physical and biochemical barriers to axonal regrowth. Therefore, effectively regulating pathological scar formation is critical for promoting neural regeneration and functional recovery.

Recent studies have increasingly focused on molecular targets involved in scar regulation. CD36, a multifunctional transmembrane receptor primarily known for its roles in lipid metabolism and immune responses, has also been implicated in tissue fibrosis [14, 15]. After SCI, CD36 is expressed in microglia, macrophages, and endothelial cells, where it promotes the release of pro-inflammatory cytokines and reactive oxygen species (ROS), exacerbating neural injury [16]. Gong *et al.* demonstrated that CD36 deletion not only reduced inflammatory marker expression but also facilitated the polarization of microglia from a pro-inflammatory M1 phenotype to an anti-inflammatory M2 phenotype, contributing to repair and neuroprotection [17, 18]. Additionally, emerging evidence suggests that CD36 interacts with the transcription factor Jun to initiate fibrotic processes; excessive Jun activation drives aberrant scar formation, while CD36 inhibition abrogates this effect [17]. These findings suggest that targeting the Jun-CD36 signaling pathway during the acute phase of SCI may offer an effective strategy for suppressing fibrotic scarring.

This study investigated the effects of pharmacological inhibition of CD36 and c-Jun on scar formation after SCI. Salvianolic acid B (SAB), a naturally derived CD36 inhibitor with established neuroprotective effects in various models [19], and T5224, a selective AP-1 (Jun) inhibitor with broad therapeutic potential in inflammatory and fibrotic diseases, were selected [20–24]. Using high-throughput sequencing and histological analyses, this study assessed the impact of SAB and T5224 on scar area, vascularization, and axonal regeneration in SCI models, while further elucidating the role of the c-Jun–Irf8–CD36 signaling axis in regulating fibrotic processes. Our findings indicate that targeting this axis can suppress fibrotic scarring during the early phase of SCI, creating a more permissive environment for axonal regeneration and lesion bridging during the chronic phase. This work introduces a novel therapeutic strategy for central nervous system repair, ultimately improving functional recovery and quality of life for patients with SCI.

Methods

Molecular docking

The receptor protein studied was CD36 (PDB ID: AF-Q08857-F1), with its three-dimensional structure obtained from the Protein Data Bank (PDB). The protein structure was visualized using PyMOL 2.5.4 to assess its suitability for molecular docking. The ligand, SAB, was modeled using InDraw and optimized with the MMFF94 force field in OpenBabel 3.1.1 to generate the lowest-energy conformer. Hydrogen atoms were added to the protein structure with AutoDock Tools 1.5.6, and the ligand underwent hydrogenation and flexible torsion adjustments. The docking grid parameters were defined using the Grid module to set the binding pocket, and a semi-flexible docking protocol was employed. The docking precision (exhaustiveness) was set to 25, with the Lamarckian genetic algorithm applied. Molecular docking was carried out with AutoDock Vina 1.2.0, producing binding free energy values and docking output files.

SCI and drug treatment

Female C57BL/6 J mice ($n = 5$ per random group) were anesthetized with tribromoethanol to ensure complete sedation and analgesia throughout the procedure. SCI was induced at the T10 vertebral level. After exposing the T10 vertebra, a right hemisection of the spinal cord was performed using a fine surgical blade. The wound was then closed by suturing the muscle and skin layers. Postoperative monitoring was conducted to assess potential discomfort, infection, or complications. Mice were randomly assigned to treatment or control groups. In the treatment groups, 100 μl of SAB (Sigma), at concentrations of 50, 100, or 200 μg/ml in saline, was administered daily by intraperitoneal injection [16, 25]. T5224 (10 mg/kg or 20 mg/kg in polyvinylpyrrolidone solution, MCE) was administered daily by oral gavage [20, 26, 27]. Drug administration began immediately after the mice regained consciousness post-surgery and continued during the early phase (the initial 14 days) following injury. Control mice received an equivalent volume of the corresponding vehicle for the same duration. All animal procedures were approved by the Animal Care and Use Committee and conducted in accordance with institutional guidelines (Approval No. P20230307-025).

Immunofluorescence of mouse spinal cord tissue

Mice were anesthetized with intraperitoneal tribromoethanol, followed by transcardial perfusion with phosphate-buffered saline (PBS) and 4% paraformaldehyde (PFA). The spinal cords were dissected, post-fixed, and cryoprotected in 30% sucrose at 4°C for 48 h. Tissue sections were cut, mounted on glass slides, and incubated with immunofluorescence blocking buffer for 1 h to prevent nonspecific antibody binding. Sections were then incubated overnight at 4°C with primary antibodies: anti-βIII Tubulin (Cell Signaling, 1:400), anti-GFAP (Abcam), anti-CD31 (R&D, 1:200), or anti-CD36 (BD Biosciences, 1:100). After washing with PBS, sections were incubated with appropriate fluorescent secondary antibodies (Donkey anti-Goat IgG (H + L) Alexa Fluor 488, Sheep anti-Mouse IgG Alexa Fluor 647, Goat anti-Chicken IgY (H + L) Alexa Fluor 488, or Sheep anti-Rabbit IgG Alexa Fluor 647; all 1:500, Invitrogen). Slides were treated with mounting medium containing DAPI (Beyotime Biotechnology) and imaged using an upright fluorescence microscope (Leica).

For multiple immunofluorescence staining, tyramide signal amplification fluorescent dye kits and digital scanners for tissue sections were purchased from Servicebio Co., Ltd (Wuhan, China).

Activated fibroblast culture

Briefly, fibrotic scar tissues collected from 14 dpi were separated and cut into small pieces. These tissue fragments were transferred to a tube containing 2 ml of 0.1% collagenase type I (Sigma,

Downloaded from academic.oup.com/burnstrauma/article/doi/10.1093/burnst/tkag020/8516470 by guest on 12 October 2026

St. Louis, MO) for digestion at 37°C for 30 min. Following digestion, the precipitated material was resuspended in fibroblast culture medium consisting of DMEM/F12 (Invitrogen) supplemented with 10% FBS, 10 ng/ml TGF-β (RD Systems, Inc., Tustin, CA), and 50 U/ml penicillin and 50 U/ml streptomycin (Beyotime). The cells were then plated onto polylysine-coated culture flasks. Once the cell confluence reached 90%, the cells were shaken at 220 rpm for 24 h.

For fibrotic phenotype analysis, fibroblasts were transfected with plasmids (Genechem Co., Ltd, Shanghai, China) or siRNAs (Ribobio, Guangzhou, China) using Lipofectamine RNAiMAX reverse transfection reagent (Invitrogen), following the manufacturer's instructions. After overnight incubation with the transfection reagent (12 h), fibroblasts were transferred to fresh culture medium and incubated for an additional 60 h or 24 h, depending on the experiment. T5224 (10 μm, MCE) and PMA (100 ng/ml, MCE) were added into the fibroblast culture medium following the established protocols [27–29].

Western blot

For protein extraction, tissue samples and cells were lysed in RIPA buffer (Beyotime) containing protease inhibitors. Protein concentration was determined using a BCA assay, and equal protein amounts were separated by sodium dodecyl sulfate-polyacrylamide gel electrophoresis and transferred to PVDF membranes. After blocking for 1 h with 5% non-fat milk at room temperature, membranes were incubated overnight at 4°C with primary antibodies: P4HB (Abcam, ab137110; 1:1000), TGF-β (Selleck, F162402; 1:1000), CD36 (Proteintech, 66395-1-Ig; 1:2000), and Postn (Biorbyt, orb385615; 1:1000), with GAPDH (Beyotime, AF0006; 1:5000) as the internal reference. After 1 h of incubation with HRP-labeled secondary antibodies, protein signals were detected using the Amersham ECL detection system, and the intensity was quantified using ImageJ software.

Behavioral assessment of motor function in mice

Basso mouse scale scoring

Mice were placed on an open-field runway and allowed to move freely for 3 min while hindlimb locomotion was observed and video recorded. Scoring was conducted under double-blind conditions by two independent observers. To ensure familiarity with the testing environment, animals underwent daily training for three days prior to surgery. Post-injury assessments were performed at designated time points to evaluate locomotor recovery.

Horizontal ladder test

SCI mice were placed on a horizontal ladder apparatus and allowed to traverse spontaneously. The number of right hindlimb foot slips and the total number of steps taken were recorded via video analysis. The error rate of the right hindlimb was calculated as the ratio of slips to total steps.

Rotarod fatigue test

Prior to testing, mice were acclimated to the behavioral testing room for at least 1 h to minimize stress. Animals received one or more training sessions before surgery and testing to minimize variability due to learning effects. During training, mice were placed on the rotarod at a constant speed. For the formal test, an accelerating protocol was used, with the rotation speed gradually increasing to a maximum of 40 rpm/min over 5 min. The latency to fall was recorded, with each animal undergoing 3–5 trials and receiving adequate rest between trials to avoid fatigue.

Single-cell suspension preparation and library construction

For tissue collection, mice were anesthetized with a fast-acting intraperitoneal anesthetic, shaved, and disinfected under sterile conditions. The animals were positioned on a sterile surgical platform, and the spinal cord was localized at the T10 level. A 2-cm segment centered on T10 was dissected and immediately transferred to pre-chilled PBS. Using a stereomicroscope, the spinal cord tissue was carefully isolated. For injured mice, a 3-mm segment encompassing the lesion site (1.5 mm rostral and 1.5 mm caudal to the injury epicenter) was rapidly harvested, while an equivalent segment was collected from sham controls. The samples were rinsed with pre-cooled PBS and placed in ice-cold tissue preservation solution. The tissue was minced into $\sim$1 mm^3 fragments with sterile surgical blades, suspended in 5 ml digestion buffer, and incubated in a 37°C water bath with agitation for 45 min. Single-cell suspensions were then processed by Shanghai Biotechnology Corporation using the Chromium Controller (10x Genomics), following the manufacturer's protocol. Single-cell 3′ gene expression libraries were prepared using the Chromium Next GEM Single Cell 3′ Kit v3.1 (10x Genomics, 1000268) and Chromium Next GEM Chip G Kit (10x Genomics, 1000120). The cell suspensions were loaded into the Chromium Controller, where single cells were partitioned into Gel Bead-in-Emulsions (GEMs). Within individual GEMs, cell lysis released RNA, which was reverse transcribed and barcoded. Libraries were sequenced on a NovaSeq 6000 platform (Illumina, San Diego, CA, USA). Highly variable genes (top 3000) were identified and subjected to principal component analysis (PCA). Clustering was performed using the *FindNeighbors* and *FindClusters* functions (resolution = 0.3). Visualization was conducted using UMAP and t-SNE. Differentially expressed genes (DEGs) across clusters were identified using the *Seurat FindMarkers* function with the Wilcoxon rank-sum test. Cell types and subpopulations were annotated based on characteristic marker genes and expression patterns.

CosMx spatial molecular imager-based spatial transcriptomics of spinal cord injury

Spatial transcriptomic profiling was performed on FFPE sections using the NanoString CosMx SMI platform (National Engineering Center for Biochip, Shanghai, China). Following target retrieval (100°C, 15 min) and Proteinase K digestion (3μg/ml, 40°C, 30 min), 386 FOVs were imaged, and *in-situ* transcripts were generated by decoding UV-cleavable fluorescent barcodes. Cell segmentation was executed via the Cellpose algorithm. Data analysis, including Leiden clustering and InsituType-based cell annotation, was conducted using Seurat (v5.0.3), scanpy (v1.9.8), and Giotto (v4.0.5).

Downloaded from academic.oup.com/burnstrauma/article/doi/10.1093/burnst/tkag020/8516470 by guest on 12 October 2026

Spatial interactions were further quantified through Delaunay networks and cell proximity enrichment analysis.

Dual-luciferase reporter assay

HEK293T cells (7×10 [5]) were seeded into 24-well plates and cultured at 37°C with 5% CO_2 until reaching 60%–70% confluence. Transfection was carried out using Lipofectamine™ 3000 (Thermo Fisher Scientific) following the manufacturer's instructions. After 24 h of transfection with Irf8 overexpression plasmids (Genechem Co., Ltd), luciferase activity was measured. Cells were washed with PBS after removal of the culture medium, then lysed with 100 μl of 1 $\times$ Passive Lysis Buffer (PLB, diluted from 5 $\times$ stock) and gently shaken at room temperature for 15 min. Lysates were collected, centrifuged at 1300 rpm for 5 min, and the supernatants transferred to fresh microcentrifuge tubes. Luciferase Assay Reagent II (LAR II) was freshly prepared by reconstituting the lyophilized substrate supplied in the kit, and the Stop & Glo® substrate was diluted 1:50 with Stop & Glo® buffer just before use. Luciferase activity was measured using a luminometer according to the manufacturer's protocol. Data were analyzed using the dual-luciferase reporter assay system (Promega).

Ribonucleic acid isolation, reverse transcription, and quantitative real-time polymerase chain reaction

RNA was extracted from cells using QIAzol reagent (Qiagen) following the manufacturer's instructions, and total RNA was purified with the RNeasy Lipid Tissue Kit (Qiagen). Genomic DNA was removed by treating the RNA with DNase I (Qiagen). Next, 1 μg of RNA was reverse transcribed using random hexamer primers (Promega) and the Omniscript RT Kit (Qiagen), with RNase inhibitor (Roche) added at a final concentration of 1 U/μl to prevent RNA degradation. Glyceraldehyde-3-phosphate dehydrogenase (GAPDH) served as the internal control.

Statistical analysis

Data were analyzed using GraphPad Prism 8.0 software. Results are expressed as mean $\pm$ standard error of the mean (SEM). Statistical comparisons between two groups were performed using Student's *t*-test, while one-way analysis of variance (ANOVA) was used for multiple group comparisons. A *P*-value of $<.05$ was considered statistically significant.

Results

Single-cell and spatial transcriptomic analysis of CD36 expression and fibrotic progression in spinal cord injury scars

Although glial scars provide neuroprotection in the acute phase of SCI by isolating the lesion site, their progression into fibrosis results in dense ECM deposition, forming a physical barrier that impedes neural repair [30]. This structure not only obstructs axonal extension mechanically but also releases inhibitory molecules such as CSPGs, creating a microenvironment that hinders neural regeneration and significantly impairs recovery in the chronic phase [12, 31]. Building on our previous research, 10x Genomics Visium spatial transcriptomic profiling was performed on spinal cord tissues from 8-week-old female C57BL/6 mice at 3, 7, 14, and 28 days after right hemisection at T10. Progressive fibrotic development of the glial scar was observed (Figure 1a) [16, 32]. Notably, CD36 expression extensively overlapped with fibroblast populations in the scar region, suggesting a potential role for CD36 in fibrotic progression (Figure 1b). To further localize CD36 within scar fibroblasts, immunostaining was conducted with P4HB, a fibroblast marker. Co-localization of $CD36^+$ regions with fibroblasts in the scar tissue was confirmed (Figure 1c, Figure S1a). Subsequently, single-cell RNA sequencing was performed on 3-mm spinal cord segments centered on the lesion at 14 dpi in 8-week-old female mice (Figure 1d). Cell type proportion analysis revealed a significant increase in fibroblast abundance, accompanied by a decrease in astrocytes, consistent with prior reports (Figure 1e). UMAP visualization, utilizing CellMarker and canonical marker genes from published studies as references (Figure S1b), identified 11 major cell types, with fibroblasts showing a marked expansion by Day 14 post-injury (Figure 1f). Further reclustering of fibroblasts into 11 subclusters (Figure 1g) revealed upregulation of CD36 in several of these subpopulations following SCI (Figure 1h and i). Specific analysis showed CD36 expression predominantly in clusters 0, 1, 2, 3, 4, and 10 (Figure 1j, Figure S1c). Although CD36 was expressed in a relatively small proportion of fibroblasts, its average expression level was notably high, corroborating our spatial transcriptomic findings in fibrotic scars (Figure 1k). These results provide compelling evidence for targeting CD36 to mitigate fibrotic scarring in SCI.

SAB targets CD36 to attenuate fibrosis in SCI scars

Recent studies have indicated that SAB can target CD36, potentially influencing central nervous system disorders [17, 19]. To investigate the interaction between SAB and CD36, molecular docking analysis was performed. The results revealed that SAB formed seven hydrogen bonds (yellow dashed lines) with amino acid residues GLY-199, VAL-208, ASP-270, SER-269, LYS-334, and GLU-335 of CD36, with a binding energy of <-5 kcal·mol^{-1}, suggesting strong binding affinity and a potential effect of SAB on CD36's structural function and bioactivity (Figure 2a). Building on this, this study examined whether SAB could inhibit CD36 and alleviate glial scar fibrosis following SCI. Mice with a right hemisection at T10 received intraperitoneal injections of SAB at three concentrations (50, 100, and 200 μg/ml) during the acute phase (Figure 2b). Notably, both treatment groups exhibited significant downregulation of CD36 expression and a marked reduction in $P4HB^+$ fibroblast populations within the fibrotic scar compared to controls (Figure 2c–f). Scar fibrosis was significantly inhibited in the 100 μg/ml SAB group, while only limited effects were observed in the 50 μg/ml SAB group. Interestingly, the 200 μg/ml SAB group showed worsened scar repair in some cases (Figure 2e and f, S2a). This phenomenon aligns with the current understanding of fibroblast roles in scar formation. During glial scar formation, fibroblasts play a protective and bridging role for surviving neural tissue in the early stages of injury, but they inhibit axonal regeneration in the chronic phase. Consequently,

Downloaded from academic.oup.com/burnstrauma/article/doi/10.1093/burnst/tkag020/8516470 by guest on 12 October 2026

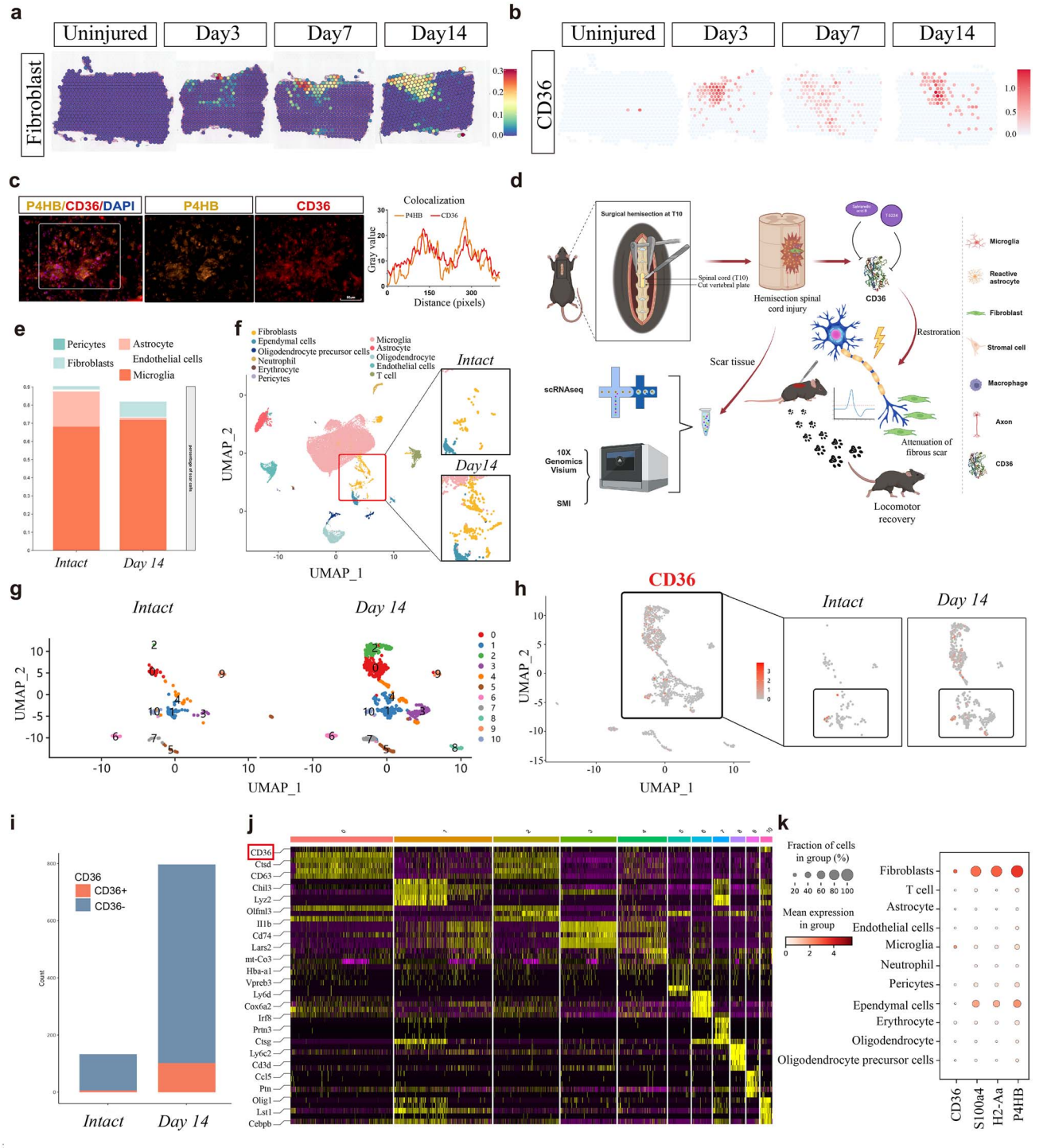


Figure 1 Spatial transcriptomic and quantitative analysis of fibroblast subpopulations and CD36 expression following SCI. (**a** and **b**) Spatial mapping of fibroblast clusters and CD36 expression at different dpi. (**c**) Elevated CD36 expression at the lesion site (scale bar: 50 μm). (**d**) Experimental design schematic used to assess the role of CD36 in SCI. (**e** and **f**) UMAP visualization of fibroblast clusters and temporal dynamics of their relative proportions; 14-day post-spinal cord injury (pSCI14d). (**g**) UMAP representation showing the identification of eleven distinct fibroblast subclusters. (**h**) Spatial mapping of CD36 expression across fibroblast subclusters. (**i**) Bar plot illustrate changes in the proportion of CD36-expressing fibroblasts between intact and SCI-14d groups. (**j**) Heatmap displaying representative marker gene expression across fibroblast subclusters. (**k**) Comparative analysis of CD36 expression levels across different cell populations; pSCI14d. *SCI* spinal cord injury

Downloaded from academic.oup.com/burnstrauma/article/doi/10.1093/burnst/tkag020/8516470 by guest on 12 October 2026

complete inhibition of fibroblasts within the glial scar impedes SCI repair. An optimal drug concentration that appropriately modulates fibroblast activity benefits SCI repair [33, 34]. Subsequent experiments focused on the 100 μg/ml SAB concentration. To assess the lasting effects of SAB intervention, fibrotic scarring was evaluated six weeks after treatment withdrawal. Scar tissue remained significantly attenuated, with long-term inhibition of fibrosis positively correlating with CD36 suppression (Figure S2b–f). These results suggest that early targeting of CD36 may provide sustained benefits for SCI repair. Given that SCI induces progressive tissue loss, partly due to vascular dysfunction and neuronal vulnerability to hypoperfusion and ischemia [35, 36], angiogenesis was examined in SAB-treated mice. Enhanced CD31 signals were observed in the SAB-treated group compared to controls (Figure 2g and h). Additionally, considering that axonal damage is a reliable predictor of functional deficits following CNS trauma, this study assessed axon regeneration. Both SAB-treated groups exhibited some axon regrowth around the scar periphery, while such regrowth was rarely detected in controls (Figure 2i and j). These results demonstrate that SAB suppresses CD36 expression, mitigates fibrotic progression, promotes neuronal survival and axon regeneration, and exerts neuroprotective effects following SCI.

T5224 targets c-Jun inhibition and promotes early functional recovery after SCI

Based on our previous 10x Genomics Visium spatial transcriptomic data, it is hypothesized that the transcription factor c-Jun regulates CD36 and contributes to fibrotic scar formation [16]. Binding motif prediction using the JASPAR database confirmed potential c-Jun-CD36 interactions, and a dual-luciferase reporter assay demonstrated that c-Jun positively regulates CD36 expression (Figure 3a and b). To validate these findings *in vivo*, the c-Jun-specific inhibitor T5224 was administered to mice subjected to right hemisection at the T10 spinal level (Figure 3c). Animals were randomized into groups and treated with oral gavage of T5224 at 10 mg/kg or 20 mg/kg daily for initial 14 days [20]. At the end of the treatment period (Day 14), scar tissues from the lesion core were collected for CosMx™ Spatial Molecular Imager (SMI) and single-cell RNA sequencing to characterize microenvironmental changes.

Both datasets revealed significant alterations in cellular composition, with a marked reduction in fibroblasts and microglia in the T5224-treated group compared to the pSCI-14d group (Figure 3e, Figure S3a and b). Additionally, the population of CD36-positive cells was decreased (Figure S3c and d). Reclustering of fibroblasts showed a reduction in most fibroblast subsets after T5224 treatment, except for subclusters 7, 8, and 9 (Figure 3d), consistent with the distribution patterns of CD36, suggesting that c-Jun regulates scar fibrosis through CD36. Immunofluorescence analysis of control scar tissues confirmed that both c-Jun and CD36 were highly expressed and co-localized within the fibrotic scars (Figure 3f). Further immunostaining of T5224-treated groups revealed a dose-dependent suppression of CD36 expression, with significant reductions compared to untreated controls (Figure 3g and h). Consistent with CD36 inhibition, fibrosis was also attenuated: P4HB$^+$ fibroblasts were significantly reduced, while GFAP$^+$ astrocytes increased in the scar region (Figure 3i). Quantitative analysis demonstrated that the 20 mg/kg group exhibited the most pronounced therapeutic effect, with significant inhibition of fibrotic scarring (Figure 3j, Figure S3e). Given these results, subsequent analyses focused on the 20 mg/kg treatment group. Angiogenesis is critical for providing nutrients and oxygen to the lesion site during the early phase of SCI, supporting neuronal survival and regeneration [37, 38]. CD31 immunostaining revealed a significant increase in vascular density within the scar tissue of the T5224-treated group, with the 20 mg/kg cohort showing the most robust angiogenic response compared to controls (Figure 3k and l). To explore the cellular basis of this angiogenic response, sub-clustering and functional enrichment analysis of endothelial cells were performed. Nine distinct subclusters were identified via t-SNE visualization (Figure S8a). Subcluster analysis revealed that Cluster 0 was significantly enriched in pathways related to angiogenesis and endothelial cell migration, driving vascular remodeling. Additionally, Cluster 1 and Cluster 4 showed high activity in ribosome biogenesis and cytoplasmic translation, indicating an elevated metabolic state necessary for protein synthesis during vessel repair. Notably, T5224 treatment significantly expanded these pro-angiogenic endothelial cell populations compared to the untreated SCI group. These results suggest that T5224 not only suppresses fibrotic scarring but also reprograms the endothelial microenvironment by activating specific endothelial cell subclusters involved in angiogenesis and structural remodeling, thereby promoting tissue revascularization and neural recovery (Figure S8b–j). To assess neuronal recovery, Tuj1 immunostaining revealed significant axon regeneration near the lesion site in the 20 mg/kg group compared to controls at 14 dpi (Figure 3m and n). These findings demonstrate that pharmacological inhibition of c-Jun with T5224 effectively downregulates CD36 expression, suppresses fibrotic scar formation, enhances angiogenesis, and promotes neuronal survival and axonal regeneration during the early phase of SCI.

Inhibition of CD36 expression promotes functional recovery after SCI

To systematically assess the effects of CD36 and its upstream regulator c-Jun on motor function after SCI, longitudinal behavioral analyses were performed at multiple time points (7, 14, 28, and 56 dpi) in both experimental and control groups (Figure 4a). Using the standardized Basso mouse scale (BMS), locomotor recovery was observed from Day 7 across all groups. The 100 μg/ml SAB-treated group exhibited significantly greater recovery compared to both the control and 200 μg/ml groups, ultimately achieving BMS scores of 7–8 (Figure 4b). Consistently, horizontal ladder and rotarod fatigue tests revealed that the SAB-treated group showed a marked reduction in coordination errors, prolonged latency to fall, and increased critical rotation speed, though these improvements did not reach statistical significance (Figure 4c–e). Based on these results, the 100 μg/ml SAB treatment group was selected for further evaluation using the TSE MotoRater system six weeks after treatment cessation (Figure S4a). At 8 weeks post-SCI, the treatment group demonstrated significantly improved range of motion in the hip, knee, and ankle joints compared to controls, with all improvements reaching statistical significance except for the ankle joint (Figure 4f and h). Given the regulatory role of c-Jun on CD36 signaling, the effects of T5224 were next

Downloaded from academic.oup.com/burnstrauma/article/doi/10.1093/burnst/tkag020/8516470 by guest on 12 October 2026

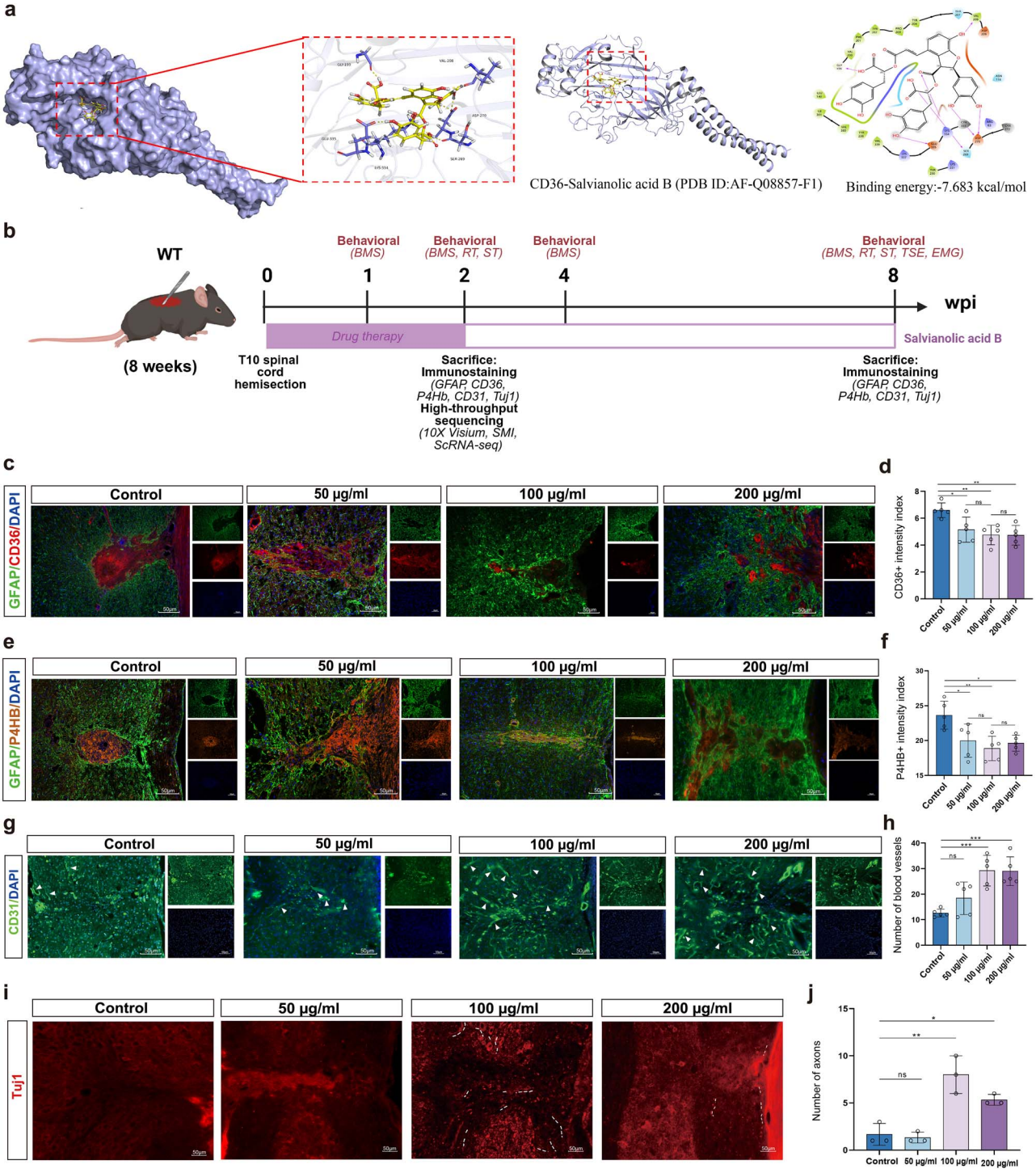


Figure 2 SAB inhibits CD36 expression and attenuates fibrotic scar after SCI. (**a**) Molecular docking analysis of SAB binding with CD36, showing multiple hydrogen bond interactions from computational modeling. (**b**) Timeline of SAB pharmacological intervention after spinal cord injury. (c and d) Reduced CD36 expression in the scar core at Day 14 post-SCI following SAB treatment (scale bar: 50 μm; $^{*}P < 0.05$, $^{**}P < 0.01$). (**e** and **f**) Decreased accumulation of P4HB^{+} fibroblasts in the scar region after SAB administration (scale bar: 50 μm; $^{*}P < 0.05$, $^{**}P < 0.01$). (**g** and **h**) Enhanced vascularization within the scar area at 8 weeks post-SCI in SAB-treated mice (scale bar: 50 μm; $^{**}P < 0.01$, $^{***}P < 0.001$). (**i** and **j**) Increased axonal reconnection around the lesion site at 8 weeks post-SCI in SAB-treated mice (scale bar: 50 μm; $^{*}P < 0.05$, $^{**}P < 0.01$). *SAB* salvianolic acid B, *SCI* spinal cord injury

Downloaded from academic.oup.com/burnstrauma/article/doi/10.1093/burnst/tkag020/8516470 by guest on 12 October 2026

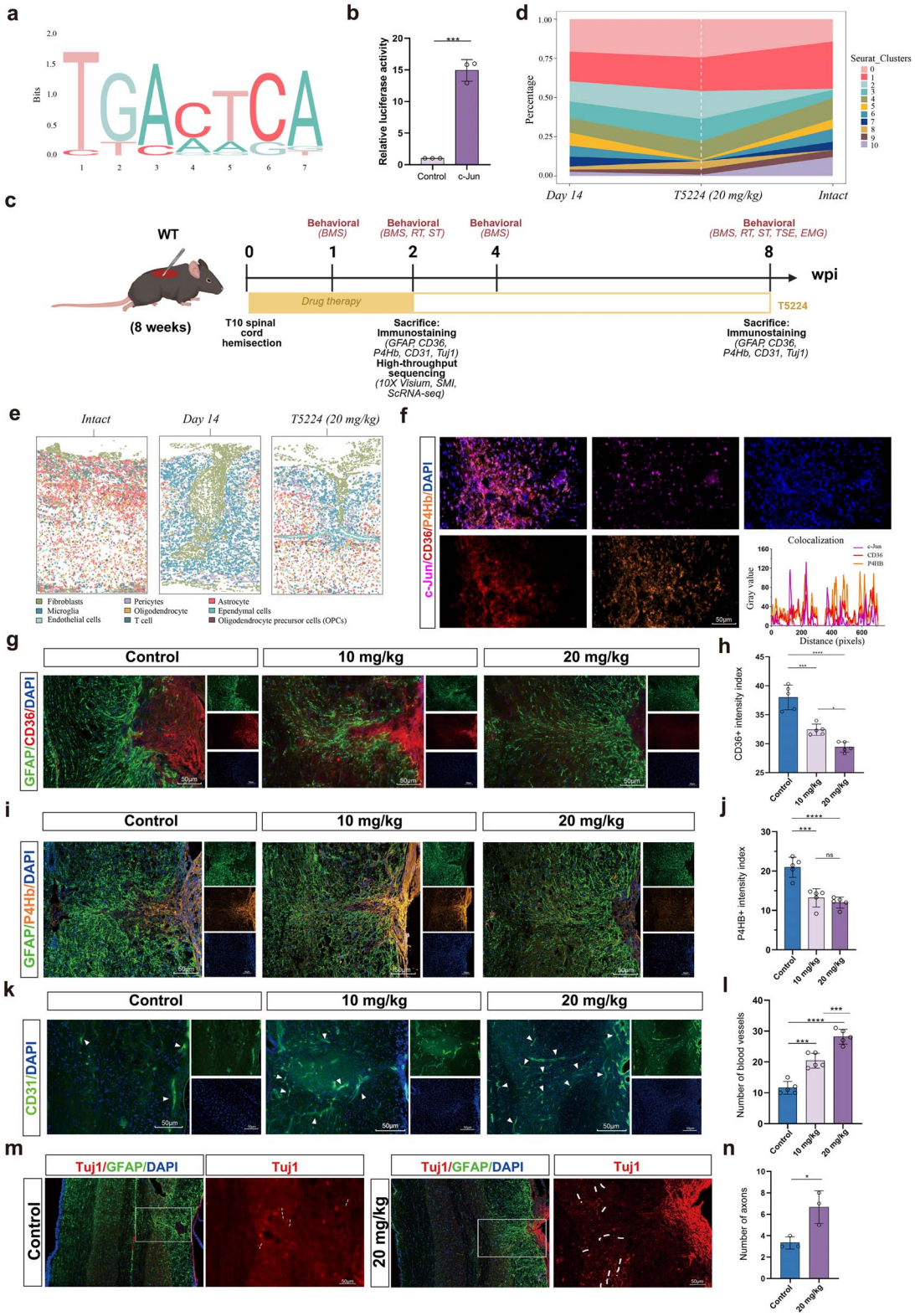


Figure 3 T5224 suppresses CD36 expression via Jun inhibition and promotes repair after SCI. (**a**) Predicted Jun-binding motif identified using the JASPAR database. (**b**) Dual-luciferase reporter assay confirming Jun-dependent transcriptional activation of CD36 (***$P < 0.001$). (**c**) Timeline of T5224 pharmacological intervention after spinal cord injury. (**d**) Comparative analysis of cellular composition in intact; pSCI14d, and T5224 20 mg/kg group. (**e**) Spatial transcriptomic analysis reveals cell-type composition and spatial distribution differences at the spinal cord lesion site after 14 days between intact (non-injured) group, pSCI-14d group and T5224 treatment group. (**f**) Immunofluorescence images showing co-localization of P4HB, CD36, and c-Jun within scar tissue. (**g** and **h**) CD36 expression significantly reduced at Day 14 post-SCI following T5224 administration (scale bar: 50 μm; *$P < 0.05$, ***$P < 0.001$, ****$P < 0.0001$). (**i** and **j**) Attenuation of fibrotic scar formation in T5224-treated groups (scale bar: 50 μm; ***$P < 0.001$, ****$P < 0.0001$). (**k** and **l**) Increased vascular density within the scar region at Day 14 post-SCI in T5224-treated mice (scale bar: 50 μm; ***$P < 0.001$, ****$P < 0.0001$). (**m** and **n**) Enhanced axonal regeneration in the 20 mg/kg T5224 group at Day 14 post-SCI, demonstrated by Tuj1 staining. Red = axons (Tuj1); green = glial cells (GFAP); white dashed lines = axon labeling (scale bar: 50 μm; *$P < 0.05$); pSCI14d. *SCI* spinal cord injury

Downloaded from academic.oup.com/burnstrauma/article/doi/10.1093/burnst/tkag020/8516470 by guest on 12 October 2026

evaluated. TSE analysis revealed substantial improvements in hip, knee, and ankle joint mobility after treatment (Figure 4g and i; Figure S4b). BMS scoring showed that the 20 mg/kg T5224 group exhibited functional recovery as early as Day 7, with both the 10 mg/kg and 20 mg/kg groups demonstrating significantly higher scores than controls at Day 14 (Figure 4j). At Day 14, the 20 mg/kg group also exhibited significantly prolonged rotarod latency to fall ($P < .05$), increased critical rotation speed ($P < .05$), and reduced horizontal ladder error rates ($P < .05$), indicating enhanced motor coordination and weight-bearing capacity (Figure 4k–m). Notably, electromyography (EMG) at Day 56 revealed no motor evoked potentials (MEPs) in the gastrocnemius muscle of control mice, while clear MEPs (amplitude: 0.42 ± 0.07 mV) were recorded in the T5224-treated group (Figure 4n and o), suggesting partial reconstruction of descending motor pathways. Histological analysis of liver and kidney tissues confirmed that T5224 treatment (20 mg/kg) did not induce pathological damage (Figure S4c), consistent with its previously reported safety profile. These results demonstrate that inhibition of c-Jun with T5224 effectively suppresses CD36 expression and significantly promotes functional recovery following SCI.

The c-Jun/Irf8/CD36 axis regulates fibrotic scar formation after SCI

To further explore the roles of c-Jun, Irf8, and CD36 in scar formation following SCI, expression patterns of these factors were first examined in a mouse SCI model. Spatial transcriptomic analysis over a time course revealed minimal expression of Cd36, c-Jun, and Irf8 in the intact spinal cord, with a marked, time-dependent accumulation specifically at the lesion site beginning at 3 dpi and peaking at 14 dpi (Figure 5a). Notably, this spatiotemporal pattern closely mirrored the distribution of classic fibrotic markers, including Col1a1, Tgfb1, and P4HB, which also exhibited concentrated expression within the injury core (Figure S5). Additionally, spatial transcriptomic mapping showed that both c-Jun and key Tgf-β signaling components (e.g. Tgfb1, Tgfbr1) accumulated in a similar pattern at the injury site, while T5224 treatment effectively reduced the expression levels of CD36 and Irf8 (Figure S7a–c). The identity of fibroblast populations was validated by the expression of characteristic markers such as Mki67 and Slc1a3 (Figure S7d). Consistent with these spatiotemporal dynamics, SCENIC analysis of fibroblast-specific transcription factors revealed a marked upregulation of c-Jun at 14 days after SCI, accompanied by increased expression of Irf8 and CD36 (Figure 5b). Analysis of upstream transcription factors specifically in $CD36^+$ fibroblast subclusters also indicated activation of both Jun and Irf8 (Figure 5c). Multiple immunofluorescence stains confirmed that the expression of c-Jun, Irf8, and CD36 was significantly upregulated following SCI, and these molecules co-localized within the fibrotic scar (Figure 5d). In cultured fibroblasts, c-Jun knockdown resulted in a significant reduction of Irf8 mRNA levels and a concurrent suppression of CD36 expression (Figure 5e). CUT&Tag assays further confirmed that Jun directly binds to the promoter region of Irf8 (Figure 5f and g). Moreover, dual-luciferase reporter assays demonstrated that Irf8 markedly enhanced CD36 promoter activity, suggesting that Irf8 positively regulates CD36 expression (Figure 5h). To investigate whether Irf8 mediates the regulatory effect of c-Jun on CD36, Irf8 was overexpressed in fibroblasts (Figure 5i). The results showed that Irf8 upregulation significantly increased CD36 expression, even under conditions of c-Jun knockdown (Figure 5j and k), indicating that Irf8 acts as a critical transcription factor conveying c-Jun signaling to CD36. To further characterize the regulatory role of the c-Jun-Irf8 axis on downstream effector molecules, Western blot analysis was performed to examine the expression of scar-associated genes, including Tgf-β, Postn, CD36, and P4HB, in cultured fibroblasts transfected with si-NC, si-c-Jun, si-c-Jun + Irf8-OE, or si-NC + Irf8-OE (Figure 5j). Consistent with previous findings, CD36 protein expression was notably reduced in the si-c-Jun group compared to the si-NC group, and this inhibitory effect was reversed by Irf8 overexpression. Moreover, Irf8 overexpression alone (si-NC + Irf8-OE) also significantly upregulated CD36 levels. A similar expression pattern was observed for Tgf-β, a key regulatory factor in fibrosis. Its protein level was decreased by c-Jun knockdown and restored or further elevated by Irf8 overexpression. In contrast, the protein expression of Postn and P4HB showed no significant differences across the four groups (Figure 5k). Furthermore, the regulatory relationship was verified by using pharmacological modulators of c-Jun. Treatment with the c-Jun agonist PMA significantly increased the expression of CD36. In contrast, the c-Jun inhibitor T5224 significantly suppressed the PMA-induced upregulation of CD36 expression (Figure S6a).

These results demonstrate that the c-Jun -Irf8 axis specifically modulates the expression of CD36 and Tgf-β, reinforcing Irf8's role as a key downstream mediator of c-Jun signaling in regulating these fibrotic markers.

Inhibition of CD36 in fibroblast populations alters gene expression and functional pathways

To assess the impact of acute-phase CD36 inhibition on fibroblast heterogeneity and repair mechanisms within the SCI scar microenvironment, differential gene expression analysis was conducted across fibroblast subclusters (Figure S6b), followed by an examination of their biological implications. Gene Ontology (GO) and Kyoto Encyclopedia of Genes and Genomes (KEGG) enrichment analyses revealed that DEGs in fibroblasts after SCI were primarily involved in processes such as cytoplasmic translation and ribonucleoprotein complex assembly, indicating significant activation of protein synthesis pathways (Figure 6a). This suggests that fibroblasts were highly active, synthesizing structural proteins, receptors, and cytokines essential for repair processes, including cell migration, ECM secretion, and signal transduction [39]. At the cellular component level, enrichment in ribosomes and ribosomal subunits further indicated enhanced translational mechanisms to facilitate rapid injury response (Figure 6a–c). Increased ribosomal activity likely accelerates the production of functional proteins, such as growth factors, collagens, and integrins, thus promoting tissue repair or scar formation. In terms of molecular function, enrichment in ribosomal structural constituents and rRNA binding confirmed active translation, likely facilitating the selective translation of mRNAs for repair-associated proteins (e.g. TGF-β, PDGF, VEGF), enhancing neuroprotection and tissue remodeling. In contrast, following

Downloaded from academic.oup.com/burnstrauma/article/doi/10.1093/burnst/tkag020/8516470 by guest on 12 October 2026

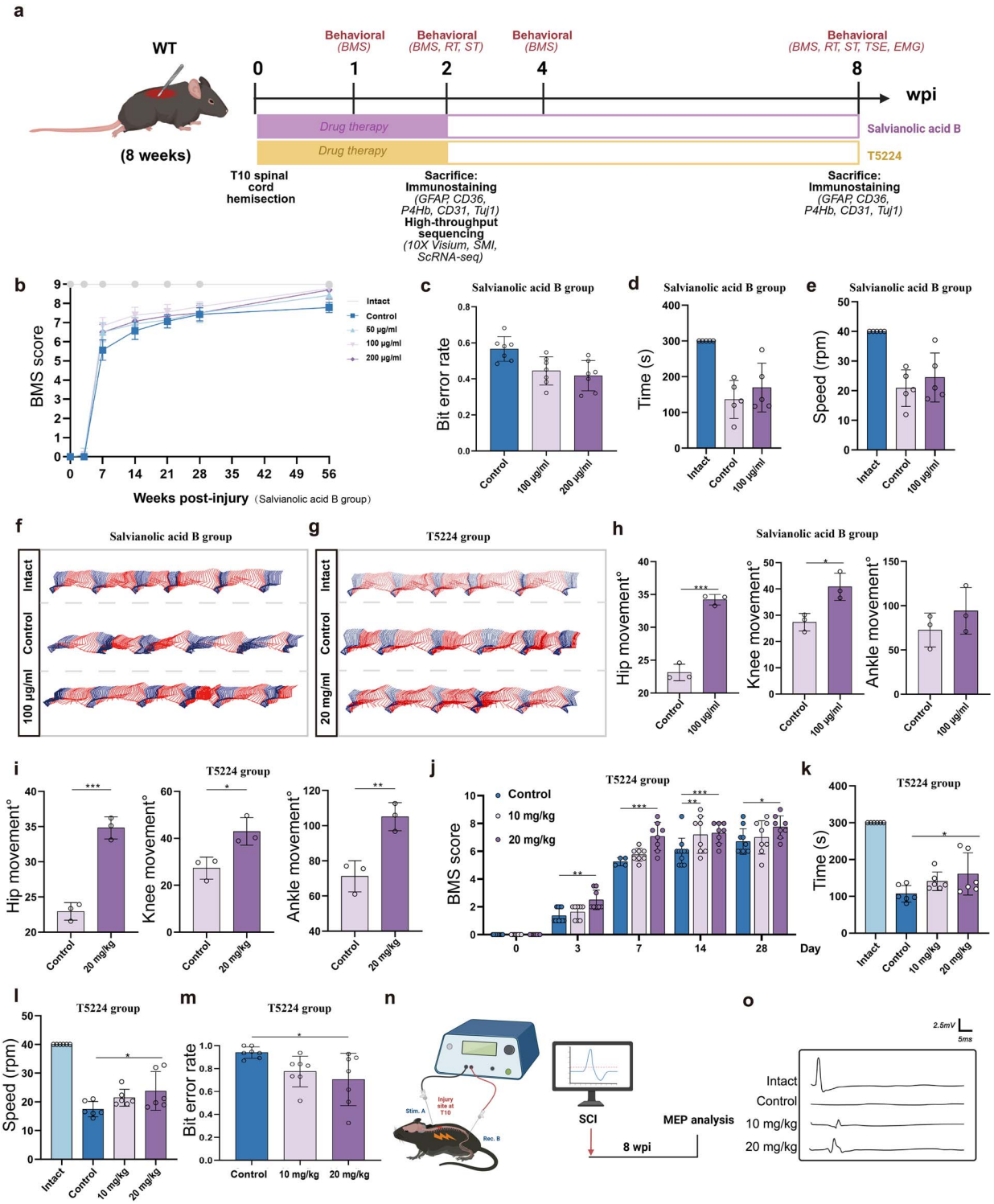


Figure 4 Behavioral recovery of motor function in spinal cord-injured mice following inhibition of CD36 expression. (**a**) Timeline of behavioral assessments conducted after SCI. (**b**) BMS scores evaluating hindlimb locomotion in SAB-treated mice at various time points post-SCI. (**c**) Horizontal ladder test demonstrating decreased foot-slip errors, indicating improved fine motor coordination in SAB-treated mice. (**d** and **e**) Rotarod fatigue test showing that SAB treatment prolongs the latency to fall and increases the critical rotational speed. (**f**) TSE MotoRater kinematic analysis of hindlimb joint angles in SAB-treated mice. (**g**) TSE MotoRater kinematic analysis of hindlimb joint angles in T5224-treated mice. (**h**) Assessment of hindlimb range of motion in knee, ankle, and hip joints by TSE MotoRater at 8 weeks post-SCI in SAB-treated mice ($^{*}P < 0.05$, $^{***}P < 0.001$). (**i**) Assessment of hindlimb range of motion in knee, ankle, and hip joints by TSE MotoRater at 8 weeks post-SCI in T5224-treated mice ($^{*}P < 0.05$, $^{**}P < 0.01$, $^{***}P < 0.001$). (**j**) BMS scores of hindlimb locomotion in T5224-treated mice at similar time intervals ($^{*}P < 0.05$, $^{**}P < 0.01$, $^{***}P < 0.001$). (**k**) Rotarod test results for T5224-treated mice, showing prolonged latency to fall and elevated critical rotation speed ($P < 0.05$ *vs* control). (**l** and **m**) Horizontal ladder analysis indicating reduced stepping errors in T5224-treated mice ($^{*}P < 0.05$). (**n** and **o**) EMG recordings show restoration of MEPs in T5224-treated mice. *SAB* salvianolic acid B, *SCI* spinal cord injury

Downloaded from academic.oup.com/burnstrauma/article/doi/10.1093/burnst/tkag020/8516470 by guest on 12 October 2026

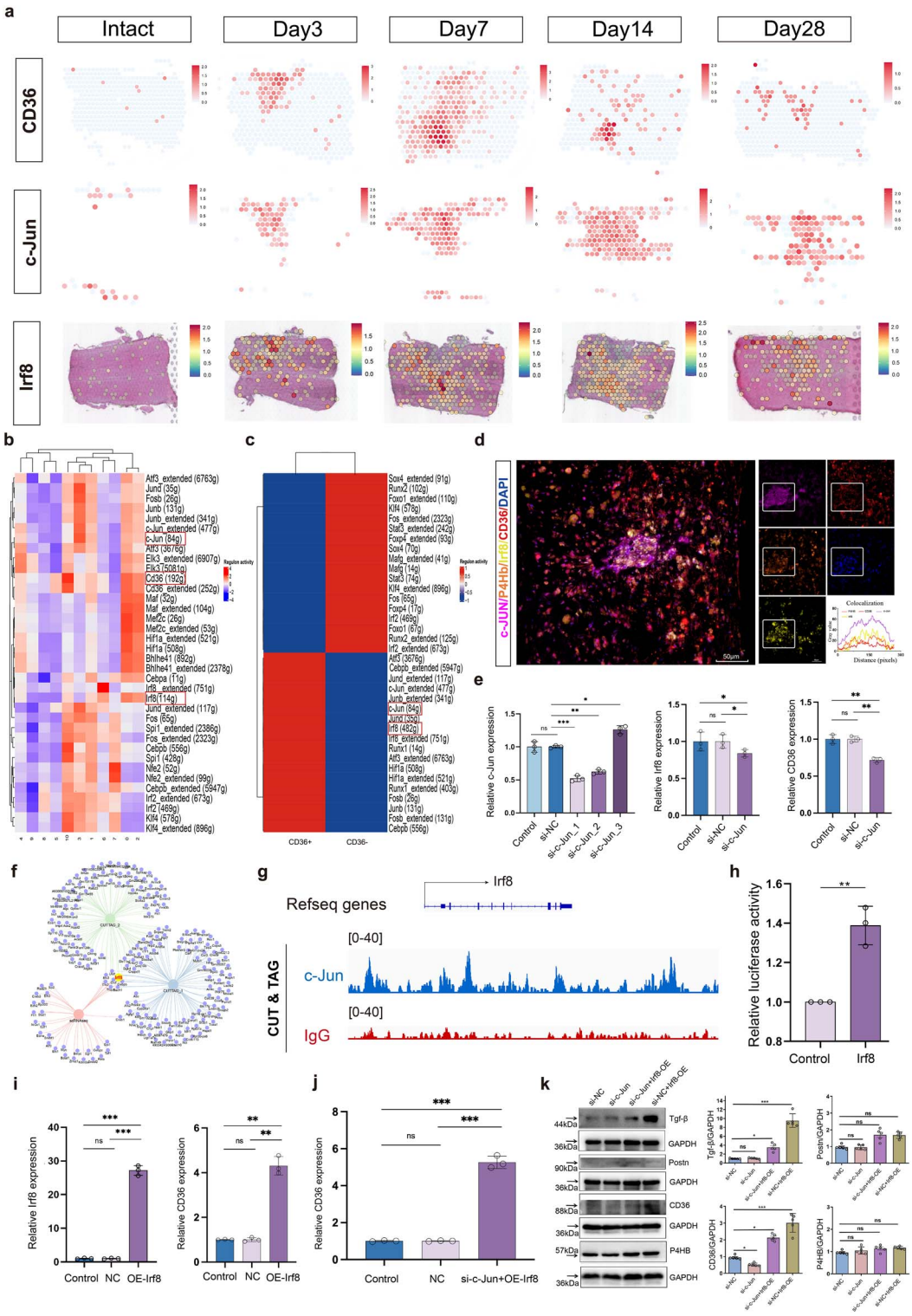


Figure 5 The c-Jun-Irf8–CD36 axis regulates fibrotic scar formation after SCI. (**a**) Spatiotemporal dynamic expression heatmaps of Cd36, c-Jun, and Irf8 after SCI. (**b**) SCENIC analysis of fibroblast-specific transcription factors showing significant upregulation of Jun during the acute phase of SCI, accompanied by concurrent increases in Irf8 and CD36. (**c**) Analysis of upstream transcription factors in $CD36^{+}$ fibroblast subclusters indicating activation of Jun and Irf8. (**d**) Immunofluorescence images confirming upregulation and co-localization of Jun, Irf8, and CD36 within the scar region post-SCI. (**e**) c-Jun knockdown in cultured fibroblasts reduced Irf8 mRNA levels and suppressed CD36 expression. siRNA-c-Jun-1(si-c-Jun-1) has the highest interference efficiency. All subsequent experiments used this si-c-Jun-1 ($^{*}P < 0.05$, $^{**}P < 0.01$, $^{***}P < 0.001$). (**f** and **g**) CUT&tag assays validating that Jun directly binds to the promoter region of Irf8. (**h**) Dual-luciferase reporter assays demonstrating that Irf8 significantly enhanced CD36 promoter activity ($^{**}P < 0.01$). (**i** and **j**) Overexpression of Irf8 in fibroblasts promoted CD36 expression, even under Jun knockdown conditions ($^{**}P < 0.01$, $^{***}P < 0.001$). (**k**) Western blot analysis of Tgf-β, Postn, CD36, and P4HB protein levels in cells transfected with si-NC, si-c-Jun, si-c-Jun + Irf8-OE, or si-NC + Irf8-OE, with GAPDH as a loading control. Quantitative analysis of band intensities (normalized to GAPDH) was performed using ImageJ software ($^{*}P < 0.05$, $^{***}P < 0.001$). *SCI* spinal cord injury

Downloaded from academic.oup.com/burnstrauma/article/doi/10.1093/burnst/tkag020/8516470 by guest on 12 October 2026

CD36 inhibition, DEGs were significantly enriched in immune-related pathways, such as the regulation of leukocyte adhesion and myeloid cell differentiation (Figure 6b–d), suggesting an increased recruitment of immune cells (e.g. macrophages and monocytes) to the injury site for debris clearance and the release of growth factors [40]. Fibroblast enrichment in these pathways suggests their potential role in modulating the immune microenvironment through paracrine signaling or direct differentiation. Cellular component analysis revealed an enrichment of cytosolic ribosomes and ribosomal structures, while molecular functions included protein heterodimerization activity and ATPase activity (Figure 6b). These results indicate that CD36 inhibition, particularly under T5224 treatment, may alter signaling complex composition, thereby reducing pro-inflammatory signaling and enhancing anti-inflammatory or tissue regeneration pathways (Figure 6b–d). Notably, CD36 expression was predominantly downregulated in fibroblast subclusters 4 and 10 (Figure 6e). GO and KEGG analyses indicated that Cluster 4 was involved in processes such as histone modification, RNA splicing regulation, cytokine-mediated signaling, and monocyte differentiation, with molecular function enrichment in transcription co-regulator and GTPase regulator activities. This suggests that Cluster 4 plays a role in maintaining transcriptional homeostasis, promoting anti-inflammatory responses, and supporting the synthesis of repair factors [41] (Figure 6f and g). In contrast, Cluster 10 was mainly associated with phagocytosis, cell adhesion regulation, and related processes (Figure 6h). KEGG analysis further highlighted its involvement in osteoclast differentiation, actin cytoskeleton regulation, and leukocyte transendothelial migration (Figure 6j), highlighting its role in tissue clearance, structural remodeling, and immune infiltration [42]. Pseudotime trajectory analysis divided fibroblasts into three developmental stages, with Clusters 4 and 10 primarily located at the early stages of injury response (Figure 6k, l, n, and o). Additionally, significant interactions between macrophages and pericytes were observed in the SCI microenvironment. Previous studies have shown that macrophages promote the migration of PDGFRβ^+ pericytes into the lesion core [43], where they differentiate into fibroblasts and contribute to scar formation. In cardiac inflammation models, recruitment of Ccr2$^+$ macrophages to the lesion site exacerbated fibrosis, whereas Ccr2 deficiency alleviated fibrosis and dysfunction [44]. Consistent with these findings, pseudotime DEG analysis revealed that pericyte marker Slc1a3 and chemokine receptor Ccr2 were expressed in fibroblast populations, with Ccr2 expression gradually declining over time (Figure 6i). Expression mapping further confirmed high levels of Slc1a3 and Ccr2 in fibroblast subclusters under SCI conditions, which were significantly reduced following drug treatment (Figure 6m and p). These results suggest that T5224 effectively restricts fibrosis-associated genes by inhibiting c-Jun and reprogramming functional pathways.

Heterogeneity and dynamic evolution of fibroblast population after SCI

Single-cell sequencing and spatial transcriptomic analyses have highlighted significant fibroblast heterogeneity following SCI [33]. Dividing fibroblasts rapidly expand and deposit large amounts of ECM post-injury, driving fibrotic scar formation. Meningeal fibroblasts migrate from the meninges into the lesion core, establishing an early barrier structure, while perivascular fibroblasts are activated from the perivascular niche, partially transforming into ECM-secreting cells, contributing to vascular repair and scar stabilization. These three fibroblast populations undergo dynamic temporal and spatial changes, collectively contributing to the fibrotic scar that hinders neural regeneration [45]. To explore fibroblast heterogeneity at the lesion site after SCI, single-cell sequencing data from uninjured samples, 14 dpi (pSCI 14d), and drug-treated groups were analyzed. In the uninjured spinal cord, dividing fibroblasts, meningeal fibroblasts, and perivascular fibroblasts were present at relatively low baseline levels with dispersed spatial distributions. At 14 dpi, all three fibroblast subtypes showed significant expansion, with dividing fibroblasts exhibiting the most pronounced increase. Meningeal and perivascular fibroblasts also expanded substantially and formed densely clustered populations in UMAP visualizations, indicating heightened activity during the acute-to-subacute phase of scar formation (Figure 7a and b). Spatial transcriptomics corroborated these findings, revealing that CD36 and the key fibrotic marker Col3a1 were highly concentrated and significantly upregulated at the lesion core in the pSCI 14d group (Figure 7c). In contrast, in the T5224-treated group, the overall proportions of all three fibroblast subtypes were significantly reduced compared to the pSCI 14d group, with their distribution in UMAP shifting from clustered to more dispersed, indicating restricted expansion (Figure 7d). These combined changes in cellular proportions and spatial distribution suggest that pharmacological intervention effectively suppresses the abnormal expansion and aggregation of fibroblasts after SCI, thereby alleviating fibrotic scar formation.

To further investigate the temporal and spatial dynamics of the three fibroblast populations, single-cell sequencing datasets from uninjured spinal cords and from spinal cords at various time points post-injury (0.5, 1, 3, 7, 14, 60, and 90 days) were analyzed. Significant differences and functional complementarity were observed across the three fibroblast subpopulations after SCI. GO and KEGG analyses revealed that dividing fibroblasts exhibited the most prominent features of high synthesis and immune activity. Their gene sets were significantly enriched in protein synthesis and proliferation-related processes such as cytoplasmic translation and ribosome biogenesis. Additionally, they showed significant enrichment in immune regulatory terms, including antigen processing and presentation, MHC class II protein complex assembly, and T cell differentiation (Figure 7e). KEGG analysis further revealed their strong association with immune-inflammatory diseases and infection pathways, suggesting their dual role in driving ECM accumulation and immune regulation (Figure 7f). Meningeal fibroblasts, in contrast, predominantly exhibited active migration, metabolism, and vascular regulation. Their GO terms were significantly enriched in leukocyte migration, cell chemotaxis, oxidative stress response, and ATP metabolic processes, as well as regulation of angiogenesis and vasculature development (Figure 7g). KEGG analysis indicated their involvement in energy metabolism, cytoskeletal regulation, and neurodegenerative diseases, suggesting that these fibroblasts not only serve as early barrier constructors migrating into the lesion core but also contribute to oxidative stress responses and vascular remodeling (Figure 7h). Perivascular fibroblasts, on the other hand, showed an enhanced profile of immune response and antigen presentation. Their GO terms were enriched in antigen processing and presentation, lymphocyte differentiation, leukocyte cell–cell adhesion, and mononuclear

Downloaded from academic.oup.com/burnstrauma/article/doi/10.1093/burnst/tkag020/8516470 by guest on 12 October 2026

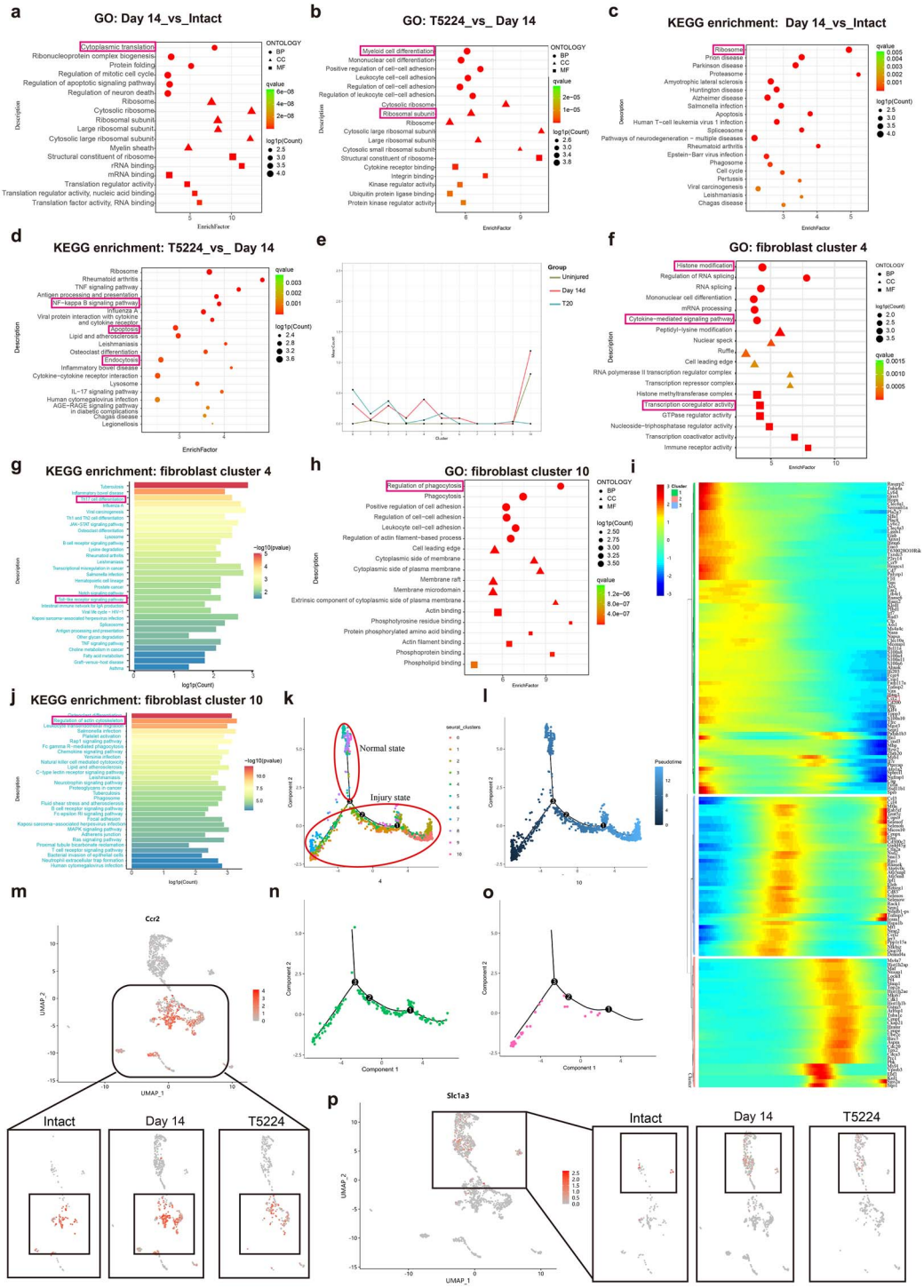


Figure 6 Heterogeneity analysis of fibroblast populations. (**a**) GO enrichment analysis of fibroblast subclusters in the SCI scar region between pSCI14d and the intact group. (**b**) GO enrichment analysis of fibroblast subclusters in the SCI scar region between the T5224 (20 mg/kg) treatment group and the pSCI14d group. (**c**) KEGG pathway enrichment analysis of fibroblast subclusters in the SCI scar region between the pSCI14d group and the intact group. (**d**) KEGG enrichment analysis of fibroblast subclusters in the SCI scar region between the T5224 (20 mg/kg) treatment and pSCI14d groups. (**e**) Expression dynamics of CD36 across fibroblast subclusters in the intact, pSCI14d, and T5224 (20 mg/kg) groups. (**f**) GO enrichment analysis of fibroblast subcluster cluster 4 in the SCI scar region. (**g**) KEGG pathway enrichment analysis of fibroblast subcluster cluster 4 in the SCI scar region. (**h**) GO enrichment analysis of fibroblast subcluster cluster 10 in the SCI scar region. (**i**) Heatmap of pseudotime-dependent DEGs, with colors ranging from red to blue indicating decreasing expression levels. (**j**) KEGG pathway enrichment analysis of fibroblast subcluster cluster 10 in the SCI scar region. (**k** and **l**) Pseudotime trajectory analysis of fibroblast subclusters. (**m**) Expression mapping of Ccr2 within fibroblast populations between the T5224 (20 mg/kg) treatment and pSCI14d groups. (**n**) Pseudotime differentiation trajectory of fibroblast subcluster cluster 4 in the SCI scar region. (**o**) Pseudotime differentiation trajectory of fibroblast subcluster cluster 10 in the SCI scar region. (**p**) Expression mapping of Slc1a3 within fibroblast populations between the T5224 (20 mg/kg) treatment and pSCI14d groups. *SCI* spinal cord injury

Downloaded from academic.oup.com/burnstrauma/article/doi/10.1093/burnst/tkag020/8516470 by guest on 12 October 2026

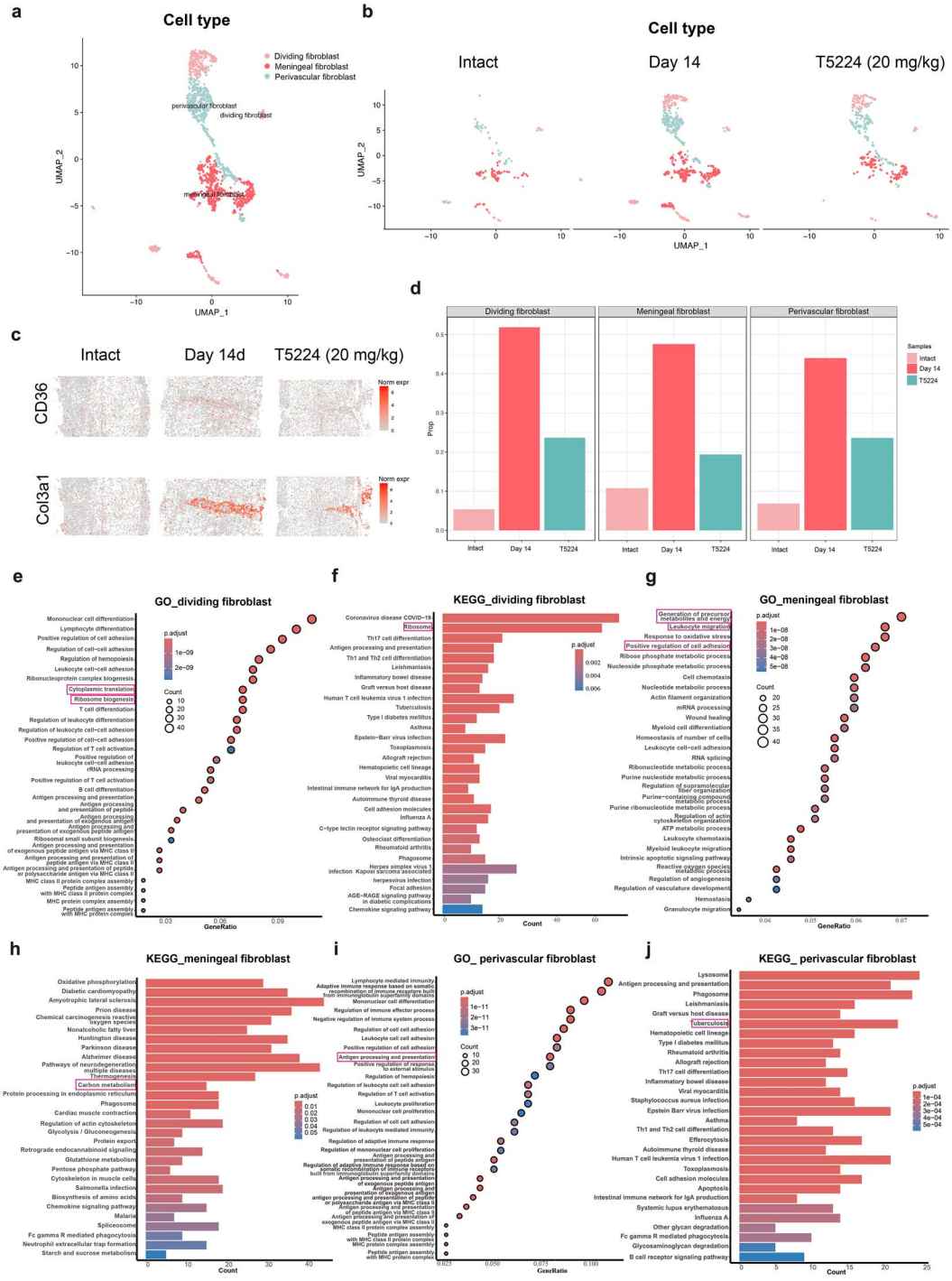


Figure 7 Distribution of fibroblast subpopulations after spinal cord injury and their GO and KEGG enrichment analyses. (**a** and **b**) UMAP visualization of the distribution of mitotic, membrane-derived, and peritubular fibroblast clusters. (**c**) Spatial transcriptomics mapping of CD36 and Col3a1 expression in the lesion areas between intact, pSCI14d and T5224 (20 mg/kg) treatment group. (**d**) Proportion changes of dividing, meningeal, and perivascular fibroblast clusters between intact, pSCI14d and T5224 (20 mg/kg) treatment group. (**e**) GO enrichment analysis showing that dividing fibroblasts were significantly enriched in protein synthesis, proliferation-related processes, and immune regulation pathways. (**f**) KEGG enrichment analysis showing the enrichment of pathways related to immune-inflammatory diseases and infection, along with strong enrichment of the ribosome pathway. (**g**) GO enrichment analysis showing that meningeal fibroblasts were enriched in leukocyte migration, cell chemotaxis, oxidative stress response, energy metabolism, and vascular regulation, including regulation of angiogenesis and vascular system development. (**h**) KEGG enrichment analysis demonstrating significant enrichment in pathways related to energy metabolism, cytoskeletal regulation, and neurodegenerative diseases, reflecting their roles in oxidative stress response and vascular remodeling. (**i**) GO enrichment analysis showing that perivascular fibroblasts are enriched in immune-related processes, including antigen processing and presentation, lymphocyte differentiation, leukocyte cell–cell adhesion, and mononuclear cell proliferation, suggesting enhanced roles in immune regulation and cell recruitment. (**j**) KEGG enrichment analysis showing significant enrichment in infection and autoimmune-related pathways

Downloaded from academic.oup.com/burnstrauma/article/doi/10.1093/burnst/tkag020/8516470 by guest on 12 October 2026

cell proliferation (Figure 7i). KEGG analysis indicated that perivascular fibroblasts were closely linked to pathways associated with autoimmune and infectious diseases, including Tuberculosis, Leishmaniasis, Systemic Lupus Erythematosus, and Rheumatoid Arthritis, suggesting their critical role in amplifying inflammation and recruiting immune cells within the scar tissue (Figure 7j). In summary, after SCI, the three fibroblast subtypes contribute to the formation of the complex fibrotic scar microenvironment through distinct roles: dividing fibroblasts drive high proliferation and immune potential, meningeal fibroblasts contribute to migration and vascular regulation, and perivascular fibroblasts amplify immune responses and inflammation [46, 47]. These processes shape the dynamic and multifaceted nature of the injury site.

Discussion

SCI is a major cause of severe neurological deficits, characterized by complex pathology involving both primary mechanical damage and secondary pathological responses. Among the latter, inflammation, oxidative stress, apoptosis, and scar formation are critical determinants of prognosis [13]. Scar tissue has long been recognized as a key barrier to axonal regeneration. Advances in research have revealed that scars are not uniform but instead consist of both glial and fibrotic components. Glial scars, primarily composed of astrocytes, play a protective role by isolating the lesion and limiting inflammation during the acute phase. However, in the chronic phase, the secretion of inhibitory molecules by astrocytes hinders axonal elongation [48]. In contrast, fibrotic scars, mainly derived from perivascular fibroblasts, persist through the deposition of collagen, fibronectin, and laminin, forming a durable physical barrier that impedes neural regeneration [49]. Consequently, reducing chronic fibrosis while preserving the acute protective functions of scar tissue has become a focal point in SCI repair research.

Recent studies have provided valuable insights into the cellular origins and molecular mechanisms underlying scar fibrosis. Fibrotic scars are predominantly derived from type A pericytes surrounding blood vessels. After SCI, these pericytes proliferate, migrate, and transdifferentiate into fibroblast-like stromal cells, contributing to ECM deposition, including fibronectin, collagen, and laminin [50]. Notably, the extradomain-A variant of fibronectin (FnEDA) has been identified as a key component in maintaining the stability of the chronic fibrotic matrix. In FnEDA-deficient mice, while acute fibrotic responses persist, long-term scarring is attenuated, axonal penetration is improved, and motor function recovery is enhanced [51]. This highlights the dual-phase regulation of scar formation: early fibrosis is essential for wound closure, whereas persistent ECM deposition ultimately inhibits regeneration [52].

The platelet-derived growth factor receptor-β (PDGFRβ) signaling pathway plays a pivotal role in fibroblast activation. PDGFRβ^+ fibroblasts and pericytes dominate the lesion core, with activation driven by PDGFB secreted by astrocytes and PDGFD released by macrophages and fibroblasts [53, 54]. Pharmacological inhibition of PDGFRβ signaling with SU16f effectively reduces fibrotic scar size, weakens scar borders, and promotes axonal regeneration and functional recovery [43, 54]. Beyond receptor tyrosine kinases, metabolic regulation has also been implicated in fibrosis. Metabolomic screening has identified nicotinamide as an inhibitor of TGFβ/SMAD signaling in fibroblasts, suppressing pro-fibrotic genes such as Col1a1, Fn1, and Acta2. In SCI mouse models, systemic administration of nicotinamide reduced fibrotic lesion area and improved motor function [55, 56]. The immune system also plays a significant role in modulating the scar microenvironment. For instance, mast cells secrete mast cell protease-6 (mMCP6), which suppresses scarring, promotes remyelination, and enhances functional outcomes in mice [56, 57]. These findings highlight that, in addition to fibroblasts and pericytes, immune cell-derived proteases can remodel the ECM, rebalancing repair and inhibition. This crosstalk between stroma and immunity provides a rationale for combining immunomodulation with antifibrotic strategies.

Fibrotic scar formation following SCI is a complex, multistep, and multicellular process involving perivascular pericytes, inflammatory mediators, ECM proteins, and metabolic regulators [33, 50, 58]. Notably, complete scar elimination can destabilize the lesion and exacerbate tissue loss, while moderate inhibition of excessive ECM deposition can maintain structural integrity and promote a favorable regenerative environment. Therefore, therapeutic strategies must strike a balance between stabilizing the lesion and optimizing conditions for regeneration. This study specifically investigated the role of CD36 during the early phase of SCI. CD36, a transmembrane glycoprotein, plays critical roles in lipid metabolism, inflammation, and fibrosis. CD36 expression was significantly upregulated in fibroblast populations within the SCI lesion. Treatment with the CD36 inhibitor SAB reduced P4HB$^+$ fibroblast accumulation, alleviated fibrotic scarring, and increased GFAP$^+$ astrocytes, suggesting a shift in scar composition. Notably, SAB treatment promoted angiogenesis, enhanced proximal axon survival, and improved motor functional recovery in mice. These findings demonstrate that CD36 plays a pivotal role in fibrotic scar formation and that its inhibition can improve the microenvironment while supporting neuroprotection.

Further single-cell transcriptomic analysis revealed that CD36 inhibition markedly reshaped the subcluster composition and functional profiles of fibroblasts within the lesion area. Both T5224 and SAB treatments significantly reduced the proportions of CD36-high subclusters 4 and 10, which were originally enriched in profibrotic pathways related to cell adhesion, signal transduction, and monocyte recruitment. Following treatment, these fibroblasts shifted toward pathways associated with immune regulation, leukocyte adhesion, phagocytosis, and energy metabolism, indicating a phenotypic transition from a profibrotic to a reparative state. Pseudotime trajectory analysis further demonstrated that CD36 inhibition restricted the abnormal proliferation and differentiation of early fibroblasts, delaying their transition into a highly activated state and thus attenuating fibrotic progression. These findings suggest that CD36 not only regulates fibroblast abundance but also dictates their functional fate and transcriptional state, playing a pivotal role in post-injury tissue remodeling.

Previous studies have identified Jun, a key member of the AP-1 family, as a broad regulator of inflammation and fibrosis. While earlier work highlighted Jun's role in fibroblast migration and collagen synthesis [59], our study is the first to reveal that Jun regulates CD36 expression through Irf8, thereby promoting SCI fibrosis. Inhibition of c-Jun or CD36 suppressed fibrotic deposition, enhanced neuroprotection and angiogenesis, and restored the balance between scar protection and axonal regeneration [19, 23, 48]. In the present study, treatment with the Jun inhibitor T5224 significantly downregulated CD36 expression, reduced fibroblast accumulation, and alleviated

Downloaded from academic.oup.com/burnstrauma/article/doi/10.1093/burnst/tkag020/8516470 by guest on 12 October 2026

scar fibrosis. Concurrently, angiogenesis and neuronal survival increased, apoptosis decreased, and functional recovery improved. Consistent with single-cell sequencing results, T5224 not only suppressed the expansion of $CD36^+$ fibroblasts but also reprogrammed their transcriptional landscape, leading to downregulation of fibrosis-associated genes (such as Tgf-β) and upregulation of genes related to immune regulation and tissue repair. These results further support the role of Jun inhibition in improving the scar microenvironment and promoting regeneration.

Compared to previous studies, our work provides novel insights into SCI fibrosis. Consistent with findings on FnEDA [51], the present study confirms that fibroblasts are central effector cells, while also identifying the c-Jun-Irf8-CD36 axis as a previously unrecognized regulatory pathway. Building on research related to PDGFRβ [50, 51], the present study further proposes an alternative mechanism of fibroblast activation, suggesting that, beyond extracellular signaling and ECM components, lipid receptors and transcription factors also play key roles in scar regulation. In contrast to studies on nicotinamide and mMCP6 [53, 54], our results demonstrate that inhibition of the c-Jun–Irf8–CD36 axis not only reduces fibrosis but also enhances angiogenesis and neuroprotection, highlighting the integrative benefits of improving the microenvironment. Tgf-β, a multifunctional cytokine, regulates cell proliferation, differentiation, and apoptosis. Upon binding to its receptors, Tgf-β activates Smad proteins and non-Smad pathways (e.g. MAPK), promoting fibrosis. In pulmonary fibrosis, the abnormal activation of the Tgf-β pathway leads to excessive ECM deposition and scar formation. Similarly, in idiopathic pulmonary fibrosis, dysregulated Tgf-β signaling is a key driver of fibrosis progression [60]. The present study observed that the c-Jun-Irf8 axis regulates Tgf-β signaling in SCI.

However, the clinical translation of several established anti-fibrotic agents, such as nintedanib, pirfenidone, and simtuzumab, still faces significant hurdles in the context of SCI. The therapeutic targets of these drugs are often either minimally expressed within the spinal fibrotic scar matrix or are inaccessible due to their poor permeability across the BBB [61–63]. Moreover, the optimal degree of fibroblast inhibition required to promote regeneration without compromising the structural integrity of the lesion remains poorly defined and warrants further investigation. Nevertheless, these compounds represent a valuable chemical library that could be explored in future studies, potentially through localized delivery systems or structural modifications to enhance CNS penetration.

Both CD36 and c-Jun are druggable targets [64–66]. SAB and T5224 already have established research foundations and clinical applications in metabolic and inflammatory diseases, with favorable pharmacokinetic and safety profiles supporting their potential for SCI treatment [67, 68]. SAB, the active component of *Salvia miltiorrhiza*, is widely used in China for treating microcirculatory diseases, including cardiovascular, cerebrovascular, and diabetes-related vascular complications [69]. T5224 has demonstrated efficacy in alleviating arthritis symptoms by inhibiting inflammatory mediators such as MMP-3 and MMP-13 induced by IL-1β. While T5224 has completed Phase II clinical trials, it is not yet widely approved for routine clinical use. Its research primarily focuses on inflammatory diseases, cancer, and cardiovascular conditions [70]. Our findings may expand the therapeutic potential of SAB and T5224, offering new avenues for SCI treatment. Furthermore, with single-cell analysis revealing fibroblast heterogeneity, future strategies could selectively target pathological fibroblast subclusters using specific markers, paving the way for precision therapies.

Nevertheless, this study has several limitations. This study relied on mouse models, and given the differences in pathology and immune context between human and mouse SCI, caution is required when extrapolating these findings to humans. Further validation in larger animal models and preclinical studies is necessary to confirm the efficacy and safety of the proposed therapeutic strategies before clinical translation. Additionally, this work primarily focused on the c-Jun–Irf8–CD36 pathway, whereas fibrotic scarring after SCI is a multifaceted process regulated by various signaling cascades, including Tgf-β/Smad, PDGFRβ, and immune-related mediators. The interactions and potential competition among these pathways remain unclear, highlighting the need for future studies integrating multi-omics approaches to establish a more comprehensive regulatory network. Although regenerated axons (as indicated by Tuj1 staining) were observed crossing the scar, it is hypothesized that these axons originated from propriospinal neurons in the spinal cord and are linked to functional recovery [71]. These hypotheses will be further validated in future studies.

Conclusions

In conclusion, this study identified the c-Jun-Irf8-CD36 signaling cascade as a central driver of fibrotic scar formation after SCI, linking transcriptional activation to the expansion and profibrotic programming of $CD36^+$ fibroblast subpopulations within the lesion core. By combining single-cell RNA sequencing with spatial transcriptomics, this study mapped CD36 enrichment in scar-associated fibroblasts and demonstrated that pharmacological blockade at two levels—direct inhibition of CD36 using SAB and upstream inhibition of c-Jun using T5224-reduces $P4HB^+$ fibroblast accumulation and matrix deposition, reshaping the scar microenvironment toward repair. Mechanistically, c-Jun promotes CD36 expression indirectly via Irf8, as confirmed by CUT&Tag and reporter assays. Pathway inhibition selectively restrains aberrantly expanded $CD36^+$ fibroblast subclusters, enhances vascular remodeling, supports axonal regeneration, and improves locomotor recovery. In conjunction with established fibrotic regulators (e.g. FnEDA, PDGFRβ, TGF-β/SMAD, and immune modulators), these findings introduce lipid receptor–associated signaling as an actionable target in SCI fibrosis and emphasize the therapeutic value of 'moderate' anti-fibrotic interventions to preserve early structural stabilization while preventing chronic regenerative blockade. This provides a compelling rationale for stage-adapted, multi-target strategies in future translational studies.

Author contributions

Min Feng (Conceptualization [equal], Data curation [lead], Formal analysis [lead], Writing—original draft [equal], Writing—review & editing [equal]), Jiyu Li (Data curation [equal], Formal analysis [equal], Project administration [equal], Software [equal], Writing—original draft [equal], Writing—review & editing [equal]), Jieying Zhang (Conceptualization [equal], Data curation [equal], Formal analysis [equal], Writing—original draft [equal]), Hang Zhang (Data curation [equal], Formal analysis [equal], Software [equal]), Yili Liu (Data curation [supporting], Software [supporting]), Xiang Gao (Data curation [supporting], Project administration [supporting], Writing—original draft [supporting]), Wanhua Li (Data

Downloaded from academic.oup.com/burnstrauma/article/doi/10.1093/burnst/tkag020/8516470 by guest on 12 October 2026

curation [supporting], Formal analysis [supporting]), Hanyue Yang (Data curation [supporting], Software [supporting]), Zeyu Liu (Data curation [supporting], Software [supporting]), Chong Gao (Resources [equal], Software [equal]), Ruiyang Xiao (Data curation [supporting]), Jianru Xiao (Data curation [supporting], Investigation [supporting], Visualization [supporting]), Xiaozhong Zhou (Project administration [supporting], Supervision [supporting]), Leilei Gong (Data curation [supporting], Funding acquisition [supporting], Investigation [supporting], Resources [supporting], Software [supporting], Supervision [supporting]), Songlin Zhou (Project administration [equal], Supervision [equal], Writing—review & editing [equal]), Jian Zhao (Formal analysis [supporting], Funding acquisition [lead], Investigation [lead], Resources [lead], Supervision [supporting]), and Caiqi Cheng (Data curation [supporting], Funding acquisition [supporting], Investigation [supporting], Writing—review & editing [supporting])

Supplementary material

Supplementary material is available at *Burns & Trauma* online.

Conflicts of interest

The authors declare no potential conflicts of interest.

Funding

This study was supported by the National Major Project of Research and Development (2022YFA1105500); the China Postdoctoral Science Foundation (2024M751997); the Shanghai Pujiang Program (23PJ1407300); the National Natural Science Foundation of China (32130060, 82302695, 82371397, 82471419 and 92368207); the Natural Science Foundation of Jiangsu Province, China (BK20232023 and BK20200976); the Fundation of Jiangsu Province Research Hospital (YJXYY202204-YBS41); the Nantong University Teaching Reform Research Project (2025B02).

Ethical approval and consent to participate

All animal procedures were approved by the Administration Committee of Experimental Animals, Jiangsu Province, China (Approval No. P20230307-025) and were conducted in accordance with institutional guidelines for animal care and use.

References

1. Ahuja CS, Nori S, Tetreault L, Wilson J, Kwon B, Harrop J, *et al.* Traumatic spinal cord injury-repair and regeneration. *Neurosurgery* 2017;80:S9–22. https://doi.org/10.1093/neuros/nyw080.
2. Badhiwala JH, Wilson JR, Witiw CD, Harrop JS, Vaccaro AR, Aarabi B, *et al.* The influence of timing of surgical decompression for acute spinal cord injury: a pooled analysis of individual patient data. *Lancet Neurol* 2021;20:117–26. https://doi.org/10.1016/S1474-4422(20)30406-3.
3. Hu X, Xu W, Ren Y, Wang Z, He X, Huang R, *et al.* Spinal cord injury: molecular mechanisms and therapeutic interventions. *Signal Transduct Target Ther* 2023;8:245. https://doi.org/10.1038/s41392-023-01477-6.
4. Eli I, Lerner DP, Ghogawala Z. Acute traumatic spinal cord injury. *Neurol Clin* 2021;39:471–88. https://doi.org/10.1016/j.ncl.2021.02.004.
5. Nie X, Wu Z, Shang J, Zhu L, Liu Y, Qi Y. Curcumol suppresses endothelial-to-mesenchymal transition via inhibiting the AKT/GSK3β signaling pathway and alleviates pulmonary arterial hypertension in rats. *Eur J Pharmacol* 2023;943:175546. https://doi.org/10.1016/j.ejphar.2023.175546.
6. Zhang W, Liu M, Ren J, Han S, Zhou X, Zhang D, *et al.* Magnetic nanoparticles and methylprednisolone based physicochemical bifunctional neural stem cells delivery system for spinal cord injury repair. *Adv Sci (Weinh)* 2024;11:e2308993. https://doi.org/10.1002/advs.202308993.
7. Adegeest CY, Ter Wengel PV, Peul WC. Traumatic spinal cord injury: acute phase treatment in critical care. *Curr Opin Crit Care* 2023;29:659–65. https://doi.org/10.1097/MCC.0000000000001110.
8. Zhang Y, Yang S, Liu C, Han X, Gu X, Zhou S. Deciphering glial scar after spinal cord injury. *Burns Trauma* 2021;9:tkab035. https://doi.org/10.1093/burnst/tkab035.
9. Tran AP, Warren PM, Silver J. The biology of regeneration failure and success after spinal cord injury. *Physiol Rev* 2018;98:881–917. https://doi.org/10.1152/physrev.00017.2017.
10. O'Shea TM, Ao Y, Wang S, Ren Y, Cheng AL, Kawaguchi R, *et al.* Derivation and transcriptional reprogramming of border-forming wound repair astrocytes after spinal cord injury or stroke in mice. *Nat Neurosci* 2024;27:1505–21. https://doi.org/10.1038/s41593-024-01684-6.
11. Zhang C, Kang J, Zhang X, Zhang Y, Huang N, Ning B. Spatiotemporal dynamics of the cellular components involved in glial scar formation following spinal cord injury. *Biomed Pharmacother* 2022;153:113500. https://doi.org/10.1016/j.biopha.2022.113500.
12. Bradbury EJ, Burnside ER. Moving beyond the glial scar for spinal cord repair. *Nat Commun* 2019;10:3879. https://doi.org/10.1038/s41467-019-11707-7.
13. Dias DO, Kalkitsas J, Kelahmetoglu Y, Estrada CP, Tatarishvili J, Holl D, *et al.* Pericyte-derived fibrotic scarring is conserved across diverse central nervous system lesions. *Nat Commun* 2021;12:5501. https://doi.org/10.1038/s41467-021-25585-5.
14. Ouyang P, Cai Z, Peng J, Lin S, Chen X, Chen C, *et al.* SELENOK-dependent CD36 palmitoylation regulates microglial functions and aβ phagocytosis. *Redox Biol* 2024;70:103064. https://doi.org/10.1016/j.redox.2024.103064.
15. Wang B-N, du AY, Chen XH, Huang T, Mamun AA, Li P, *et al.* Inhibition of CD36 ameliorates mouse spinal cord injury by accelerating microglial lipophagy. *Acta Pharmacol Sin* 2025;46:1205–20. https://doi.org/10.1038/s41401-024-01463-w.
16. Gong L, Gu Y, Han X, Luan C, Liu C, Wang X, *et al.* Spatiotemporal dynamics of the molecular expression pattern and intercellular interactions in the glial scar response to spinal cord injury. *Neurosci Bull* 2023;39:213–44. https://doi.org/10.1007/s12264-022-00897-8.
17. Kim E, Yang J, Woo Park K, Cho S. Preventative, but not post-stroke, inhibition of CD36 attenuates brain swelling in hyperlipidemic stroke. *J Cereb Blood Flow Metab* 2020;40:885–94. https://doi.org/10.1177/0271678X19850004.

Downloaded from academic.oup.com/burnstrauma/article/doi/10.1093/burnst/tkag020/8516470 by guest on 12 October 2026

18. Borrell-Pages M, Luquero A, Vilahur G, Padró T, Badimon L. Canonical Wnt pathway and the LDL receptor superfamily in neuronal cholesterol homeostasis and function. *Cardiovasc Res* 2024;120:140–51. https://doi.org/10.1093/cvr/cvad159.
19. Cho S. CD36 as a therapeutic target for endothelial dysfunction in stroke. *Curr Pharm Des* 2012;18:3721–30. https://doi.org/10.2174/138161212802002760.
20. Zhang H, Pei L, Ouyang Z, Wang H, Chen X, Jiang K, *et al.* AP-1 activation mediates post-natal cardiomyocyte maturation. *Cardiovasc Res* 2023;119:536–50. https://doi.org/10.1093/cvr/cvac088.
21. Ye N, Ding Y, Wild C, Shen Q, Zhou J. Small molecule inhibitors targeting activator protein 1 (AP-1). *J Med Chem* 2014;57:6930–48. https://doi.org/10.1021/jm5004733.
22. Zaman SU, Pagare PP, Huang B, Rilee G, Ma Z, Zhang Y, *et al.* Novel PROTAC probes targeting FOSL1 degradation to eliminate head and neck squamous cell carcinoma cancer stem cells. *Bioorg Chem* 2024;151:107613. https://doi.org/10.1016/j.bioorg.2024.107613.
23. Sasakura M, Urakami H, Tachibana K, Ikeda K, Hasui KI, Matsuda Y, *et al.* Topical application of activator protein-1 inhibitor T-5224 suppresses inflammation and improves skin barrier function in a murine atopic dermatitis-like dermatitis. *Allergol Int* 2024;73:323–31. https://doi.org/10.1016/j.alit.2023.12.006.
24. Foster DS, Guo JL, Meany E, Berry CE, Fallah M, Korah M, *et al.* Postoperative adhesions are abrogated by a sustained-release anti-JUN therapeutic in preclinical models. *Sci Transl Med* 2025;17:eadp9957. https://doi.org/10.1126/scitranslmed.adp9957.
25. Zhu Z, Ding L, Qiu W-F, Wu H-F, Li R. Salvianolic acid B protects the myelin sheath around injured spinal cord axons. *Neural Regen Res* 2016;11:487–92. https://doi.org/10.4103/1673-5374.179068.
26. Izuta S, Ueki M, Ueno M, Nishina K, Shiozawa S, Maekawa N. T-5224, a selective inhibitor of c-Fos/activator protein-1, attenuates lipopolysaccharide-induced liver injury in mice. *Biotechnol Lett* 2012;34:2175–82. https://doi.org/10.1007/s10529-012-1022-4.
27. Kamide D, Yamashita T, Araki K, Tomifuji M, Tanaka Y, Tanaka S, *et al.* Selective activator protein-1 inhibitor T-5224 prevents lymph node metastasis in an oral cancer model. *Cancer Sci* 2016;107:666–73. https://doi.org/10.1111/cas.12914.
28. Schwende H, Fitzke E, Ambs P, Dieter P. Differences in the state of differentiation of THP-1 cells induced by phorbol ester and 1,25-dihydroxyvitamin D3. *J Leukoc Biol* 1996;59:555–61. https://doi.org/10.1002/jlb.59.4.555.
29. Starr T, Bauler TJ, Malik-Kale P, Steele-Mortimer O. The phorbol 12-myristate-13-acetate differentiation protocol is critical to the interaction of THP-1 macrophages with salmonella typhimurium. *PLoS One* 2018;13:e0193601. https://doi.org/10.1371/journal.pone.0193601.
30. Anderson MA, O'Shea TM, Burda JE, Ao Y, Barlatey SL, Bernstein AM, *et al.* Required growth facilitators propel axon regeneration across complete spinal cord injury. *Nature* 2018;561:396–400. https://doi.org/10.1038/s41586-018-0467-6.
31. Clifford T, Finkel Z, Rodriguez B, Joseph A, Cai L. Current advancements in spinal cord injury research-glial scar formation and neural regeneration. *Cells* 2023;12:853. https://doi.org/10.3390/cells12060853.
32. Hou J, Bi H, Ge Q, Teng H, Wan G, Yu B, *et al.* Heterogeneity analysis of astrocytes following spinal cord injury at single-cell resolution. *FASEB J* 2022;36:e22442. https://doi.org/10.1096/fj.202200463R.
33. Xue X, Wu X, Fan Y, Han S, Zhang H, Sun Y, *et al.* Heterogeneous fibroblasts contribute to fibrotic scar formation after spinal cord injury in mice and monkeys. *Nat Commun* 2024;15:6321. https://doi.org/10.1038/s41467-024-50564-x.
34. Holl D, Hau WF, Julien A, Banitalebi S, Kalkitsas J, Savant S, *et al.* Distinct origin and region-dependent contribution of stromal fibroblasts to fibrosis following traumatic injury in mice. *Nat Neurosci* 2024;27:1285–98. https://doi.org/10.1038/s41593-024-01678-4.
35. Zhang Z, Guth L. Experimental spinal cord injury: Wallerian degeneration in the dorsal column is followed by revascularization, glial proliferation, and nerve regeneration. *Exp Neurol* 1997;147:159–71. https://doi.org/10.1006/exnr.1997.6590.
36. Hubertus V, Meyer L, Waldmann L, Roolfs L, Taheri N, Kersting K, *et al.* Identification of a therapeutic window for neurovascular unit repair after experimental spinal cord injury. *J Neurotrauma* 2025;42:212–28. https://doi.org/10.1089/neu.2024.0233.
37. He L, Vanlandewijck M, Mäe MA, Andrae J, Ando K, del Gaudio F, *et al.* Single-cell RNA sequencing of mouse brain and lung vascular and vessel-associated cell types. *Sci Data* 2018;5:180160. https://doi.org/10.1038/sdata.2018.160.
38. Xu J, Li P, Lu F, Chen Y, Guo Q, Yang Y. Domino reaction of neurovascular unit in neuropathic pain after spinal cord injury. *Exp Neurol* 2023;359:114273. https://doi.org/10.1016/j.expneurol.2022.114273.
39. Dong Y, Kang H, Peng R, Liu Z, Liao F, Hu SA, *et al.* A clinical-stage Nrf2 activator suppresses osteoclast differentiation via the iron-ornithine axis. *Cell Metab* 2024;36:1679–1695.e6. https://doi.org/10.1016/j.cmet.2024.03.005.
40. Zhang S, Weinberg S, DeBerge M, Gainullina A, Schipma M, Kinchen JM, *et al.* Efferocytosis fuels requirements of fatty acid oxidation and the electron transport chain to polarize macrophages for tissue repair. *Cell Metab* 2019;29:443–456.e5. https://doi.org/10.1016/j.cmet.2018.12.004.
41. Duran E, Schmidt A, Welty R, Jalihal AP, Pitchiaya S, Walter NG. Utilizing functional cell-free extracts to dissect ribonucleoprotein complex biology at single-molecule resolution. *Wiley Interdiscip Rev: RNA* 2023;14:e1787. https://doi.org/10.1002/wrna.1787.
42. Westman J, Grinstein S, Marques PE. Phagocytosis of necrotic debris at sites of injury and inflammation. *Front Immunol* 2019;10:3030. https://doi.org/10.3389/fimmu.2019.03030.
43. Li Z, Zheng M, Yu S, Yao F, Luo Y, Liu Y, *et al.* M2 macrophages promote PDGFRβ+ pericytes migration after spinal cord injury in mice via PDGFB/PDGFRβ pathway. *Front Pharmacol* 2021;12:670813. https://doi.org/10.3389/fphar.2021.670813.
44. Zhuang T, Chen MH, Wu RX, Wang J, Hu XD, Meng T, *et al.* ALKBH5-mediated m6A modification of IL-11 drives macrophage-to-myofibroblast transition and pathological cardiac fibrosis in mice. *Nat Commun* 2024;15:1995. https://doi.org/10.1038/s41467-024-46357-x.
45. Milich LM, Choi JS, Ryan C, Cerqueira SR, Benavides S, Yahn SL, *et al.* Single-cell analysis of the cellular heterogeneity and interactions in the injured mouse spinal cord. *J Exp Med* 2021;218:e20210040. https://doi.org/10.1084/jem.20210040.

Downloaded from academic.oup.com/burnstrauma/article/doi/10.1093/burnst/tkag020/8516470 by guest on 12 October 2026

46. Soderblom C, Luo X, Blumenthal E, Bray E, Lyapichev K, Ramos J, *et al.* Perivascular fibroblasts form the fibrotic scar after contusive spinal cord injury. *J Neurosci* 2013;33:13882–7. https://doi.org/10.1523/JNEUROSCI.2524-13.2013.
47. Dorrier CE, Jones HE, Pintarić L, Siegenthaler JA, Daneman R. Emerging roles for CNS fibroblasts in health, injury and disease. *Nat Rev Neurosci* 2022;23:23–34. https://doi.org/10.1038/s41583-021-00525-w.
48. Wu J, Lu B, Yang R, Chen Y, Chen X, Li Y. EphB2 knockdown decreases the formation of astroglial-fibrotic scars to promote nerve regeneration after spinal cord injury in rats. *CNS Neurosci Ther* 2021;27:714–24. https://doi.org/10.1111/cns.13641.
49. Guo J, Yang T, Zhang W, Yu K, Xu X, Li W, *et al.* Inhibition of CD44 suppresses the formation of fibrotic scar after spinal cord injury via the JAK2/STAT3 signaling pathway. *iScience* 2024;27:108935. https://doi.org/10.1016/j.isci.2024.108935.
50. Li Z, Yu S, Hu X, Li Y, You X, Tian D, *et al.* Fibrotic scar after spinal cord injury: crosstalk with other cells, cellular origin, function, and mechanism. *Front Cell Neurosci* 2021;15:720938. https://doi.org/10.3389/fncel.2021.720938.
51. Cooper JG, Jeong SJ, McGuire TL, Sharma S, Wang W, Bhattacharyya S, *et al.* Fibronectin EDA forms the chronic fibrotic scar after contusive spinal cord injury. *Neurobiol Dis* 2018;116:60–8. https://doi.org/10.1016/j.nbd.2018.04.014.
52. Ayazi M, Zivkovic S, Hammel G, Stefanovic B, Ren Y. Fibrotic scar in CNS injuries: from the cellular origins of fibroblasts to the molecular processes of fibrotic scar formation. *Cells* 2022;11:2371. https://doi.org/10.3390/cells11152371.
53. Chio JCT, Punjani N, Hejrati N, Zavvarian MM, Hong J, Fehlings MG. Extracellular matrix and oxidative stress following traumatic spinal cord injury: physiological and pathophysiological roles and opportunities for therapeutic intervention. *Antioxid Redox Signal* 2022;37:184–207. https://doi.org/10.1089/ars.2021.0120.
54. Li Z, Yu S, Liu Y, Hu X, Li Y, Xiao Z, *et al.* SU16f inhibits fibrotic scar formation and facilitates axon regeneration and locomotor function recovery after spinal cord injury by blocking the PDGFRβ pathway. *J Neuroinflammation* 2022;19:95. https://doi.org/10.1186/s12974-022-02449-3.
55. Peng Z-Z, Hu GY, Shen H, Wang L, Ning WB, Xie YY, *et al.* Fluorofenidone attenuates collagen I and transforming growth factor-beta1 expression through a nicotinamide adenine dinucleotide phosphate oxidase-dependent way in NRK-52E cells. *Nephrology (Carlton)* 2009;14:565–72. https://doi.org/10.1111/j.1440-1797.2009.01129.x.
56. Zhang C, Shao Q, Zhang Y, Liu W, Kang J, Jin Z, *et al.* Therapeutic application of nicotinamide: as a potential target for inhibiting fibrotic scar formation following spinal cord injury. *CNS Neurosci Ther* 2024;30:e14826. https://doi.org/10.1111/cns.14826.
57. Vangansewinkel T, Geurts N, Quanten K, Nelissen S, Lemmens S, Geboes L, *et al.* Mast cells promote scar remodeling and functional recovery after spinal cord injury via mouse mast cell protease 6. *FASEB J* 2016;30:2040–57. https://doi.org/10.1096/fj.201500114R.
58. Nogueira-Rodrigues J, Leite SC, Pinto-Costa R, Sousa SC, Luz LL, Sintra MA, *et al.* Rewired glycosylation activity promotes scarless regeneration and functional recovery in spiny mice after complete spinal cord transection. *Dev Cell* 2022;57:440–450.e7. https://doi.org/10.1016/j.devcel.2021.12.008.
59. Sofroniew MV. Astrocyte reactivity: subtypes, states, and functions in CNS innate immunity. *Trends Immunol* 2020;41:758–70. https://doi.org/10.1016/j.it.2020.07.004.
60. Ong CH, Tham CL, Harith HH, Firdaus N, Israf DA. TGF-β-induced fibrosis: a review on the underlying mechanism and potential therapeutic strategies. *Eur J Pharmacol* 2021;911:174510. https://doi.org/10.1016/j.ejphar.2021.174510.
61. Wollin L, Maillet I, Quesniaux V, Holweg A, Ryffel B. Antifibrotic and anti-inflammatory activity of the tyrosine kinase inhibitor nintedanib in experimental models of lung fibrosis. *J Pharmacol Exp Ther* 2014;349:209–20. https://doi.org/10.1124/jpet.113.208223.
62. Conte E, Gili E, Fruciano M, Korfei M, Fagone E, Iemmolo M, *et al.* PI3K p110γ overexpression in idiopathic pulmonary fibrosis lung tissue and fibroblast cells: *in vitro* effects of its inhibition. *Lab Investig* 2013;93:566–76. https://doi.org/10.1038/labinvest.2013.6.
63. Di Pastena F, Gautam J, JSV L, Fayyazi R, Grasset E, Bhattacharya D, *et al.* Dual inhibition of ACLY and ACSS2 by EVT0185 reduces steatosis, hepatic stellate cell activation, and fibrosis in mouse models of MASH. *Cell Metab* 2026;38:33–49.e10. https://doi.org/10.1016/j.cmet.2025.11.015.
64. Wang J, Li Y. CD36 tango in cancer: signaling pathways and functions. *Theranostics* 2019;9:4893–908. https://doi.org/10.7150/thno.36037.
65. Kim E-H, Tolhurst AT, Szeto HH, Cho S-H. Targeting CD36-mediated inflammation reduces acute brain injury in transient, but not permanent, ischemic stroke. *CNS Neurosci Ther* 2015;21:385–91. https://doi.org/10.1111/cns.12326.
66. Vogt PK. Jun, the oncoprotein. *Oncogene* 2001;20:2365–77. https://doi.org/10.1038/sj.onc.1204443.
67. Wei X-H, Chen J, Wu XF, Zhang Q, Xia GY, Chu XY, *et al.* Salvianolic acid B alleviated myocardial ischemia-reperfusion injury via modulating SIRT3-mediated crosstalk between mitochondrial ROS and NLRP3. *Phytomedicine* 2025;136:156260. https://doi.org/10.1016/j.phymed.2024.156260.
68. Zhang Z, Tao Z, Zhang Z, Zhang W, Zhang X, Xu X, *et al.* Single-cell transcriptomic analysis reveals AP-1 downregulation remodels bone marrow environment and contributes to osteopenia in ovariectomized mice. *J Orthop Translat* 2025;52:1–13. https://doi.org/10.1016/j.jot.2025.03.001.
69. He G, Chen G, Liu W, Ye D, Liu X, Liang X, *et al.* Salvianolic acid B: a review of pharmacological effects, safety, combination therapy, new dosage forms, and novel drug delivery routes. *Pharmaceutics* 2023;15:2235. https://doi.org/10.3390/pharmaceutics15092235.
70. Guryanova SV, Maksimova TV, Azova MM. Transcription factors and methods for the pharmacological correction of their activity. *Int J Mol Sci* 2025;26:6394. https://doi.org/10.3390/ijms26136394.
71. Squair JW, Milano M, de Coucy A, Gautier M, Skinnider MA, James ND, *et al.* Recovery of walking after paralysis by regenerating characterized neurons to their natural target region. *Science* 2023;381:1338–45. https://doi.org/10.1126/science.adi6412.

© The Author(s) 2026. Published by Oxford University Press. This is an Open Access article distributed under the terms of the Creative Commons Attribution-NonCommercial License (https://creativecommons.org/licenses/by-nc/4.0/), which permits non-commercial re-use, distribution, and reproduction in any medium, provided the original work is properly cited. For commercial re-use, please contact reprints@oup.com for reprints and translation rights for reprints. All other permissions can be obtained through our RightsLink service via the Permissions link on the article page on our site—for further information please contact journals.permissions@oup.com.
Burns & Trauma, 2026, 14, tkag020
https://doi.org/10.1093/burnst/tkag020
Research Article

Downloaded from academic.oup.com/burnstrauma/article/doi/10.1093/burnst/tkag020/8516470 by guest on 12 October 2026